



# 1 Photochemical and ozone-induced aging significantly alter the 2 viscosity of aqueous *trans*-aconitic acid aerosol particles

3 Cynthia Antossian<sup>1</sup>, Marcel Müller<sup>1,a</sup>, and Ulrich K. Krieger<sup>1</sup>

4 <sup>1</sup>Institute for Atmospheric and Climate Science, ETH Zurich, Universitätsstrasse 16, 8092 Zurich, Switzerland

5 <sup>a</sup>currently at: Institute of Biogeochemistry and Pollutant Dynamics, ETH Zurich, Universitätsstrasse 16, 8092  
6 Zurich, Switzerland

7  
8 Correspondence to: Ulrich K. Krieger ([ulrich.krieger@env.ethz.ch](mailto:ulrich.krieger@env.ethz.ch)) and Cynthia Antossian  
9 ([cynthia.antossian@env.ethz.ch](mailto:cynthia.antossian@env.ethz.ch))

10 **Abstract.** Aging processes of organic aerosols, including reactions with gas phase oxidants, such as ozone (O<sub>3</sub>),  
11 as well as photochemical reactions, can significantly alter their physicochemical properties. While previous  
12 research has examined how photochemical aging and ozonolysis affect the physicochemical properties of organic  
13 aerosols, our study investigates the combined effect of photolysis and ozonolysis. We use aqueous *trans*-aconitic  
14 acid as a proxy for secondary organic aerosol particles (SOA), selected for its ability to absorb UV light and for  
15 containing a C=C double bond that is susceptible to ozonolysis. We observe significant mass loss in single particles  
16 levitated in an electrodynamic balance when exposed to either O<sub>3</sub> or UV light (375 nm), as well as to both aging  
17 processes simultaneously, resulting from fragmentation reactions followed by the volatilization of some of the  
18 products. Viscosity measurements at 17% relative humidity revealed an increase of nearly 4 orders of magnitude  
19 after both UV exposure and combined UV and O<sub>3</sub> exposure at 60% mass loss. Interestingly, continued UV-aging  
20 beyond 60% mass loss resulted in a viscosity decrease, whereas combined UV and O<sub>3</sub> exposure led to a further  
21 viscosity increase. Hygroscopicity exhibited only a modest decline after 20% mass loss during UV-aging and  
22 remained constant with further UV exposure; this reduction was less pronounced when UV-aging occurred in the  
23 presence of O<sub>3</sub>. Overall, our results indicate that the mixing times within accumulation mode SOA particles may  
24 increase from 4 s to 4 h after aging under dry boundary layer conditions.

25

## 26 1 Introduction

27 Aerosol particles play a prominent role in the atmosphere, since they are involved in many important processes  
28 including cloud formation, biogeochemical cycling, and light scattering (Seinfeld and Pandis, 2016). Moreover,  
29 aerosols affect human health, since they have been associated with respiratory and cardiac diseases, oxidative  
30 stress, and cancer (Dockery and Pope, 1994; Nel, 2005). Organic compounds constitute a major fraction of  
31 atmospheric aerosols (20-90%) (Kanakidou et al., 2005; Jimenez et al., 2009). A significant fraction of these  
32 aerosols are secondary organic aerosols (SOA) (Zhang et al., 2007), which are formed when volatile organic  
33 compounds oxidize and produce compounds with low volatility that partition from the gas phase into the particle  
34 phase, eventually forming SOA (Pankow, 1994). In addition, these low volatility compounds can partition into  
35 preexisting aerosols, leading to internal mixing of primary and secondary aerosol particles (Marcolli et al., 2004;  
36 Marcolli and Krieger, 2020)

37 Throughout their lifetimes in the atmosphere, these organic aerosol particles undergo various aging processes. One  
38 of these processes are reactions with gas phase oxidants, such as ozone (O<sub>3</sub>), hydroxyl radicals (OH), and nitrate  
39 radicals (NO<sub>3</sub>). In addition to the reactions with oxidants, organic aerosols can undergo photochemical reactions  
40 due to exposure to UV or even visible light, either directly or indirectly by photosensitizers, leading to additional  
41 aging. Oxidation reactions can occur through different pathways (Kroll and Seinfeld, 2008), depending on the  
42 chemical composition of the gas and particle phase and on the atmospheric conditions, such as temperature and  
43 relative humidity (RH). For instance, fragmentation can take place because of carbon-carbon double bond  
44 cleavage, leading to more volatile products that volatilize from the particle. Functionalization can also take place  
45 because of the addition of polar functional groups, thus increasing oxygen-to-carbon ratio O:C and forming more  
46 hygroscopic, higher molecular weight products that have low volatility. In addition, oligomerization or accretion  
47 can occur through the association of small molecules, consequently forming products with similar O:C, but higher  
48 number of carbon atoms that have low hygroscopicity, low volatility, and high viscosity (Kroll and Seinfeld, 2008).  
49 Fragmentation reactions have been observed for a range of organic aerosol particles during photochemical aging  
50 or when exposed to atmospheric oxidants (O'Brien and Kroll, 2019; Sun and Smith, 2024; Dou et al., 2021; Kroll



et al., 2015). Moreover, oxidation of SOA has been shown to induce the formation of oligomers through accretion reactions e.g. (Kalberer et al., 2004). At present, it remains uncertain which mechanisms dominate under different aerosol compositions and atmospheric conditions, making it challenging to predict aerosol properties during and after aging.

These aging processes can significantly alter the physicochemical properties of organic aerosols, such as the viscosity and hygroscopicity (Hosny et al., 2016; Athanasiadis et al., 2016; Baboomian et al., 2022; Jimenez et al., 2009; Kroll et al., 2011; Kroll et al., 2015). Viscosity of organic aerosols varies over a wide range, depending on the chemical properties, such as molecular structure, functional groups, chain length, molecular weight, and carbon oxidation state and on the environmental conditions, such as temperature and relative humidity (Gou et al., 2025). Moreover, the viscosity of organic aerosols is an indication of the phase state, with aerosols having viscosity values less than  $10^2$  Pa s considered as being liquid, between  $10^2$  and  $10^{12}$  Pa s semi-solid, and greater than  $10^{12}$  Pa s solid (Shiraiwa et al., 2011; Koop et al., 2011).

Viscosity affects the condensed phase chemistry (Pöschl and Shiraiwa, 2015), gas-particle partitioning (Shiraiwa et al., 2011), and the ability of the aerosol particle to act as ice nucleating particles (Wolf et al., 2020; Murray et al., 2010), while hygroscopicity affects the ability of the particle to act as cloud condensation nuclei (Chan et al., 2008), thereby affecting the Earth's energy budget and climate. Moreover, viscosity affects the ability of the particle to react with other chemical species. Viscous aerosols can limit molecular motion due to slow diffusion of oxidants, water, and organic compounds (Pöschl and Shiraiwa, 2015). This makes particulate air pollutants less susceptible to degradation and increases their mixing times in the troposphere, thereby favoring their transport and effecting human health (Mu et al., 2018; Bastelberger et al., 2017). For instance, polycyclic aromatic hydrocarbons (PAHs) that were coated with viscous organic aerosols, were shielded from oxidation, highlighting stronger long-range transport and elevated lung cancer risk (Shrivastava et al., 2017).

Several studies have observed the change in viscosity of organic aerosols upon aging. For instance, studies on the ozonolysis of oleic acid aerosols (Hosny et al., 2016) and squalene droplets (Athanasiadis et al., 2016) indicate a significant increase in viscosity upon oxidation. SOA formed from ozonolysis of organic aerosols might also undergo additional aging, for instance photochemically, altering further the viscosity of these particles. A recent study on the photochemical aging of SOA generated from the ozonolysis of d-limonene and  $\alpha$ -pinene shows an increase of several orders of magnitude in viscosity after UV-aging, ultimately transforming into a glassy solid state, especially at low temperatures and relative humidities (Baboomian et al., 2022). However, to the best of our knowledge, it is not known how the aerosol properties, particularly viscosity and hygroscopicity, will change after simultaneous exposure to UV light and ozone.

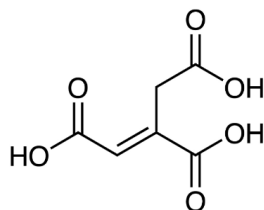
In this work, we use *trans*-aconitic acid particles as surrogate for SOA to investigate how the viscosity and hygroscopicity are influenced by different degrees and different combinations of photochemical and ozone-induced aging.

85

## 86 2 Materials, Instrumentation, and Method

### 87 2.1 Materials

*Trans*-aconitic acid (AA) is a naturally occurring tricarboxylic acid that is produced by several plants and accumulates significantly in sugar cane and sweet sorghum (Bruni and Klasson, 2022). Since it is a highly oxidized molecule having carboxyl functional groups, it has low vapor pressure, and is water soluble, we use it here as a proxy system for SOA present in the atmosphere.



92

93 Figure 1: The structure of *trans*-aconitic acid.



The UV-visible absorption spectra (Fig. 2) obtained using a UV-Visible spectrophotometer (Varian Cary 100 Bio) shows that concentrated AA solution ( $2.13 \text{ mol L}^{-1}$ ) absorbs even in the visible range of the solar spectrum, with significant absorbance at 375 nm. AA's absorbance at the visible to near UV wavelengths could be attributed to the conjugated structure of *trans*-aconitic acid, which makes it possible to undergo photochemical reaction at 375 nm illumination. Moreover, the presence of the double bond makes AA susceptible to ozonolysis. As a result of all these properties, AA was chosen in this study as a suitable proxy system for SOA for studying synergistic effects between photochemistry and ozonolysis.

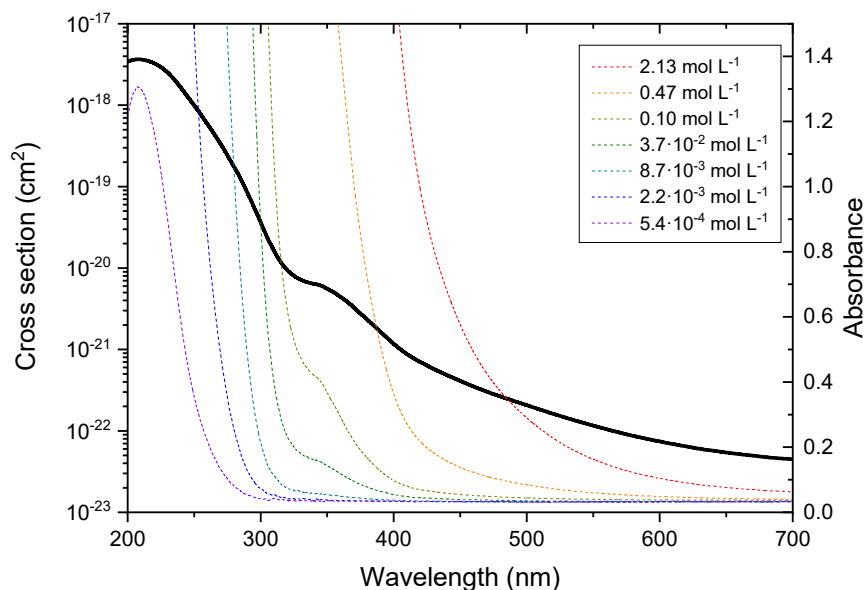


**Figure 2: Absorption spectra (colored lines) and cross section (black line) of AA solution of different concentrations as a function of wavelength (absorbance values higher than 1.5 are not shown because they are above the maximum detection limit of the instrument).**

## 2.2 Electrodynamic Balance Setup

Experiments on single, levitated, aqueous AA particles were conducted using a linear electrodynamic balance (EDB) (Fig. 3). The set-up has been described previously (Müller et al., 2022). Briefly, single aqueous AA droplets were prepared from 4 wt-% AA (98%, Sigma Aldrich) in MilliQ water and injected using a droplet on demand generator (HP-inkjet cartridge model 51604). The droplet was inductively charged and levitated in the EDB trap by AC and DC electric fields. 50 sccm of humidified flow from hydrocarbon free synthetic air (PanGas, 20% O<sub>2</sub> in N<sub>2</sub>) was used to keep RH in the EDB at 78% – 88%. All experiments were performed at room temperature (~298 K). RH and temperature were measured using two sensors (Sensirion SHT85, Switzerland) placed at the flow entrance to the EDB as well as at the flow exit of the EDB. The sensor at the flow exit is located close to the levitated particle and it was confirmed in measurements of the hygroscopic response of NaCl particles that this sensor's RH readout is close to the RH at the location of the particle. The uncertainty in RH measurement is  $\pm 1.5\%$ .

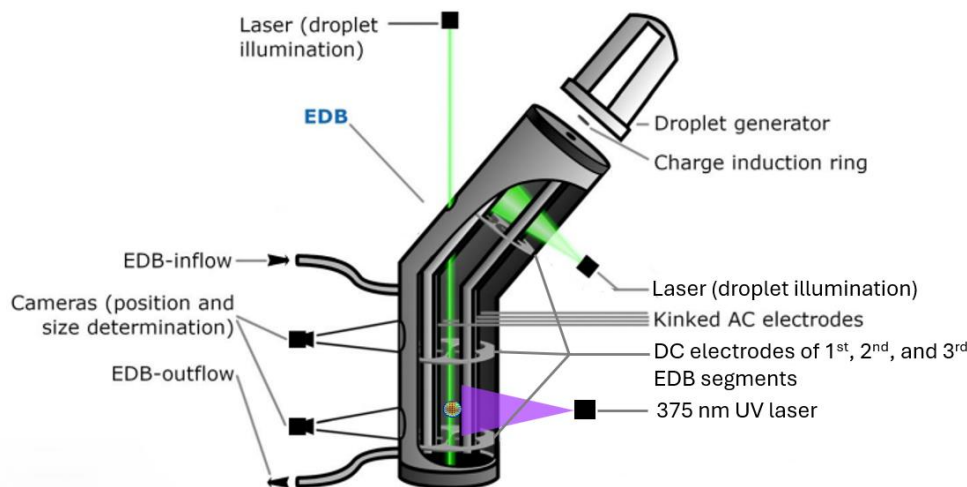
Aging experiments were conducted by exposing AA particles to 10 ppm ozone generated by UV photolysis of O<sub>2</sub> in synthetic air using an ozone generator (AOS, BMT Messtechnik, Germany). The readout of an electrochemical ozone sensor (OX-B431 on Alphasense ISB, Alphasense, UK) was used to control the ozone generator. For UV



122 exposure, the unfocused beam of a 375 nm UV laser (Omicron LuxX-20, Germany) illuminated the particle  
 123 levitated at the second segment of the EDB. Its beam profile and power lead to an irradiance at the particle location  
 124 of about  $0.16 \text{ W cm}^{-2}$ .

125 The  $\text{O}_3$  exposure used in the experiments is similar to an atmospheric exposure of 100 ppb ozone for 10 d. The  
 126 UV photon flux used in the experiments is 1 order of magnitude larger than atmospheric conditions, based on the  
 127 power density of the laser irradiation and AA absorbance together with the solar irradiance integrated over the  
 128 entire spectrum. This means that the  $\text{O}_3$  exposure and UV irradiation exposure used in our experiments are  
 129 comparable to about 10 d of exposure in the atmosphere, which is a typical lifetime of atmospheric aerosols.

130 The particle was illuminated with a 532 nm diode pumped solid state laser (Thorlabs, DJ532, USA) and the  
 131 scattered light was collected on CCD cameras (Raspberry Pi HQ camera, UK). The change in mass of the particle  
 132 was deduced by measuring the electric force needed to balance the gravitational force of the particle. The DC  
 133 voltage was adjusted by an automatic feedback loop driven by the particle image. Since in addition to the  
 134 gravitational force, the DC voltage compensates for the Stokes force of the gas flow, drag force correction was  
 135 applied to deduce changes in mass. Moreover, the size of the particle was deduced from the two-dimensional  
 136 angular optical scattering (TAOS) pattern of laser-illuminated droplets. The inverse of the fringe distance along  
 137 the symmetry axis of the TAOS pattern is a direct measure of the size; smaller size changes are detected by  
 138 following a single maximum in the TAOS pattern. Thus, the radius of the particle was deduced from the mean  
 139 distance between the fringes as long as the particle remained spherical and symmetric with regular TAOS pattern.  
 140 For detecting phase transitions breaking the spherical symmetry of the particle, we use the pattern distortion  
 141 parameter as introduced by (Braun and Krieger, 2001). More details on the radius retrieval can be found in  
 142 Appendix A.



143

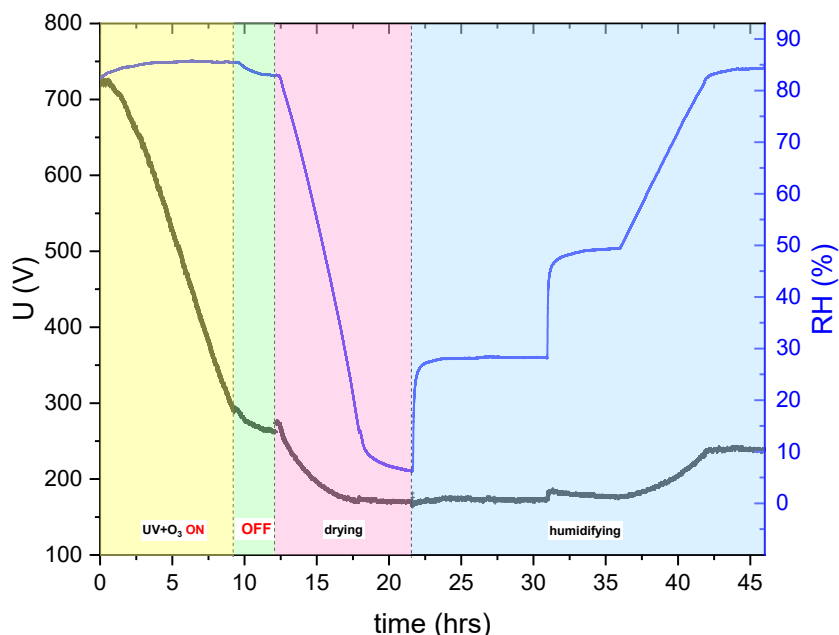
144 **Figure 3: Schematic representation of the EDB set-up, adopted with slight modifications from (Müller et al., 2022). The**  
 145 **UV laser illuminated the particle levitated at the 2<sup>nd</sup> segment of the EDB. For simplification and better representation,**  
 146 **the UV laser was shown in this figure in the 3<sup>rd</sup> segment of the EDB.**

### 147 2.3 Overview of the experimental procedure

148 Figure 4 shows an example of the experimental procedure to obtain hygroscopicity as well as viscosity for a  
 149 combined ozonolysis and photochemical aging experiment. Initially, an aqueous AA particle is injected and  
 150 levitated in the EDB. After RH is equilibrated at  $\sim 83\%$ , 375 nm UV laser and 10 ppm  $\text{O}_3$  are switched on ( $t=0$ ).  
 151 The change in mass is monitored and size measurements are done in parallel. The reaction is carried out at  
 152 approximately constant RH, and UV illumination and  $\text{O}_3$  are switched off after the particle loses 60% of its initial  
 153 mass. Since slight fluctuations in RH and temperature occur after switching off  $\text{O}_3$ , the particle is kept in the dark  
 154 until RH, and therefore the mass and size of the particle are almost constant. Kinetics of the reaction will be  
 155 discussed in Sect. 3.2. Afterwards, RH inside the EDB is decreased slowly at a rate of  $0.2\% \text{ min}^{-1}$  from  $\sim 83\%$  to  
 156  $\sim 6\%$  and then kept constant for 3.5 h to ensure sufficient drying. From this drying part of the experiment,



157 hygroscopicity is deduced, as will be explained in more detail in Sect. 2.4. Finally, RH is increased in two steps  
 158 rapidly, first from 6.3% to 28.2%, then from 28.2% to 49.4%, and finally raised back from 49.4% to 84.4% slowly.  
 159 While the flow change is indeed step-like, the response in RH is approximately exponential. The first step in  
 160 humidity was used to derive condensed phase water diffusivity, as will be discussed in more detail in Sect. 2.5.



161  
 162 **Figure 4:** Overview figure showing the complete experimental procedure of AA particle exposed to UV and O<sub>3</sub>  
 163 simultaneously until 60% mass loss at room temperature. The black line represents the voltage needed to keep the  
 164 particle levitated in the EDB (corrected for drag force), which is proportional to the mass of the particle. The blue line  
 165 represents the RH data. The yellow section corresponds to switching on UV laser and O<sub>3</sub>, the green section corresponds  
 166 to turning off UV and O<sub>3</sub>, the pink section corresponds to drying, and the blue section corresponds to humidifying.

167

## 168 2.4 Hygroscopicity measurement

169 Hygroscopicity and water diffusivity measurements were done on aged particles after they lost about 20%, 40%,  
 170 50%, 60% and 80% of their mass. For hygroscopicity measurements, RH was allowed to decrease slowly, at a rate  
 171 of 0.2% min<sup>-1</sup>, by adjusting the ratio of dry nitrogen gas flow relative to the humidified flow while keeping the  
 172 total flow constant using automatic mass flow controllers. The change in mass of the particles was monitored  
 173 during drying using the automatic feedback loop, see Fig. 4.

174 The hygroscopic size growth factor ( $G(RH)$ ) indicates the relative increase in size of the particles at a certain RH  
 175 relative to dry conditions in response to water uptake. If  $G(RH)$  is measured at different RH, a single parameter,  
 176  $\kappa$ , for hygroscopic size growth can be determined, assuming ideality (Petters and Kreidenweis, 2007):

$$177 \quad G(RH) = \frac{D(RH)}{D_0} = \left(1 + \kappa \frac{a_w}{1 - a_w}\right)^{1/3} \quad (1)$$

178 where  $D(RH)$  is the mobility diameter of the particle at a certain RH,  $D_0$  is the diameter of the particle at dry  
 179 conditions, and  $a_w$  is the water activity, which is equal to RH at equilibrium.



180 Since here the mass growth factor ( $g(RH)$ ) was measured instead of the size growth factor,  $\kappa$  can be determined  
 181 from the mass growth factor by using Eq. (2) (Zardini et al., 2008):

$$182 \quad g(RH) = \frac{m(RH)}{m_0} = 1 + ((G(RH))^3 - 1) \frac{\rho_w}{\rho_0} \quad (2)$$

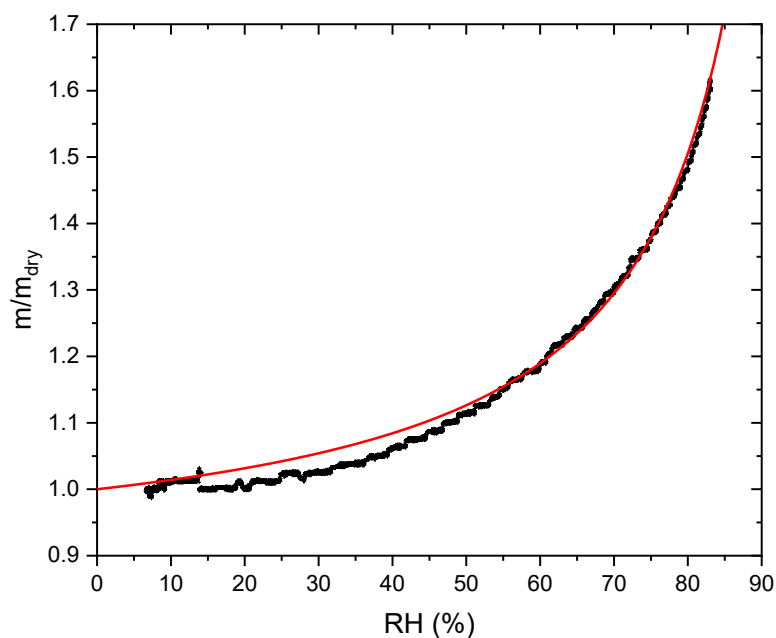
183 Combining Eq. (1) and Eq. (2) yield Eq. 3:

$$184 \quad g(RH) = 1 + \left( \kappa \frac{a_w \rho_w}{1 - a_w \rho_0} \right) \quad (3)$$

185 where  $m(RH)$  is the mass of the particle at a certain RH,  $m_0$  is the mass of the particle at dry conditions (measured  
 186 at ~6% RH),  $\rho_w$  is the density of water, and  $\rho_0$  is the density of the particle at dry conditions.  $\rho_0$  for AA was  
 187 determined experimentally using the conventional additivity rule and was found to be  $1.56 \text{ g cm}^{-3}$  and was assumed  
 188 to remain constant after aging, see Appendix B.

189 Since most untreated AA effloresced at RH 59.9%,  $\kappa$ -parametrization fitting according to Eq. (3) was done only in  
 190 the RH range 62% – 80% for all particles. Furthermore, fitting at higher RH provides a better estimation for  $\kappa$  as  
 191 deviations from ideality become less important with dilution. Figure 5 shows an example of the measured mass  
 192 growth together with a regression of Eq. (3) to deduce  $\kappa$ .

193



194

195 **Figure 5:** Mass growth factor as a function of RH for AA exposed to UV light and  $\text{O}_3$  till 60% mass loss (black line). The  
 196 red line is the  $\kappa$ -parametrization fitting in the RH range 62% – 80%, yielding a  $\kappa$  of 0.197.

197

## 198 2.5 Viscosity determination

199 Viscosity of the particles after aging was inferred indirectly by estimating the water diffusivity and then using the  
 200 fractional Stokes–Einstein relation to deduce the viscosity.



For water diffusivity measurements, the aged particles were subjected to drying and were kept under low RH (below 15%) for  $4 \pm 1$  h, until RH stabilized around 6%. Then, RH was increased rapidly from  $6.7 \pm 0.7\%$  to  $28.6 \pm 0.5\%$  and kept constant for  $9 \pm 2$  h. As RH increases, water diffuses from the gas phase into the particle phase until equilibrium between water activity throughout the particle and RH of the gas phase is reached (Koop et al., 2011). The time taken to reach equilibrium depends on the viscosity of the particle, i.e. liquid droplets will reach equilibrium faster than amorphous solid or glassy particles. Thus, water diffusivity can be inferred by observing the time response in particle mass or size following a step increase in RH (Zobrist et al., 2011; Bones et al., 2012). One way of retrieving the diffusion coefficient from such data is by using a numerical model, solving the diffusion equation (Zobrist et al., 2011; O'meara et al., 2016). Alternatively, the response of step increase in RH may be approximated by an exponential approach to the new RH setting, see data and exponential fit in Fig. 6. While a viscous liquid close to the glass transition exhibits a non-linear response leading to a non-exponential relaxation (Debenedetti and Stillinger, 2001; Rickards et al., 2015), a less viscous liquid may be reasonably well approximated by a single exponential response. Under these conditions, the hygroscopic response can be deconvoluted analytically as detailed in Appendix C. The response  $y(t)$  to the hygroscopic 'step' in either mass or size is then given by Eq. (4) with  $\tau_1$  being the characteristic time of the response we are searching for and  $\tau_2$  being the characteristic time of the RH step, induced by the flow change from dry to humidified.

$$y(t) = \left(1 - e^{-t/\tau_1}\right) - \frac{\tau_2}{\tau_2 - \tau_1} \left(e^{-t/\tau_2} - e^{-t/\tau_1}\right) \quad (4)$$

Water diffusivity can then be approximately deduced from  $\tau_1$  using the following equation (Seinfeld and Pandis, 2016; Bones et al., 2012):

$$\tau_1 = \frac{r^2}{\pi^2 D} \quad (5)$$

where  $\tau_1$  is the characteristic time,  $r$  is the radius of the particle, and  $D$  is the diffusion coefficient.

We show in Appendix D that this linear response approximation needs a correction to obtain  $D$ , such that it compares favorably with a full numerical model for water diffusivities in the range of  $1.7 \times 10^{-12} \text{ cm}^2 \text{ s}^{-1}$  to  $2 \times 10^{-9} \text{ cm}^2 \text{ s}^{-1}$  and particle sizes used in our experiment.

Viscosity can then be predicted from diffusivity using Stokes–Einstein relation (Einstein, 1905):

$$D = \frac{KT}{6\pi\eta R_{diff}} \quad (6)$$

where  $D$  is the diffusion coefficient,  $K$  is the Boltzmann constant,  $T$  is the temperature,  $\eta$  is the viscosity, and  $R_{diff}$  is the radius of the diffusing species. While this relation works well for large diffusing molecules in which the radius of the diffusing molecule ( $R_{diff}$ ) is greater than that of the organic matrix molecule ( $R_{matrix}$ ), it underestimates the diffusion coefficients in organic–water mixtures by several orders of magnitude for small diffusing molecules like water, where  $R_{diff}$  is smaller than  $R_{matrix}$  (Price et al., 2015; Bastelberger et al., 2017). A better approach to relate diffusivity to viscosity is to use fractional Stokes-Einstein relation where  $D$  is proportional to  $1/\eta^\xi$ ,  $\xi$  being the fractional exponent, which depends on the ratio  $R_{diff}/R_{matrix}$  (Evoy et al., 2020).  $\xi$  can be expressed in terms of  $R_{diff}/R_{matrix}$  according to the following empirical equation (Evoy et al., 2020):

$$\xi = 1 - [0.73 \exp(-1.79 \frac{R_{diff}}{R_{matrix}})] \quad (7)$$

The hydrodynamic radius of AA ( $R_{matrix}$ ) was assumed to be the same as that of citric acid, which is structurally similar to aconitic acid, and was taken as  $3.7 \text{ \AA}$  (Muller and Stokes, 1957) and for water the Van der Waals radius of  $1.41 \text{ \AA}$  (Pang, 2014) was used.

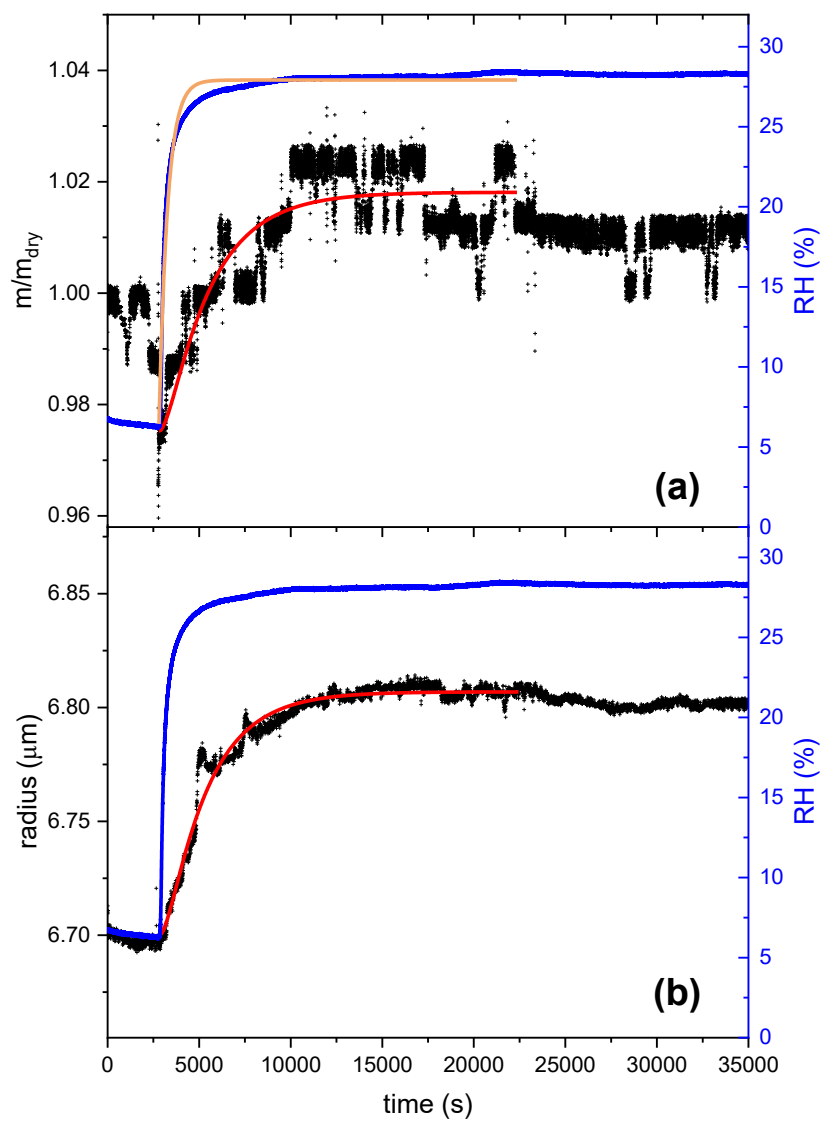






Figure 6: The response of AA to rapid changes in RH after aging with UV and O<sub>3</sub> until 60% mass loss, panel (a) shows mass growth data and panel (b) size data. The blue line in both panels shows the RH data (right scale). At time  $t = 2,804$  s, the gas flow was switched from dry to humid with RH increasing rapidly from 6.3% to 28.2% and afterwards kept constant for 7.5 h. The black lines represent the response of the aged AA particle in terms of mass (a) and size (b) to the rapid increase in RH. The orange line in panel (a) is an exponential fit to the RH data. The red lines are the first-order kinetics fitting on the mass response (a) and size (b) response. Fitting was done only up to 22,300 s because after this time the mass and size of the particle started to decrease slightly, possibly due to volatilization of some of the remaining products when RH was increased.  $\tau_2$ , determined from the RH-fit, was found to be 472 s.  $\tau_1$ , determined from the fitting according to Eq. (4), was found to be 2,503 s for the mass response and 2,312 s for the size response. Note: the step-like noise seen in the mass growth data is an artifact of the instrument, mainly due to the automatic feedback loop that adjusts the voltage to keep the particle at a fixed position, but with a finite resolution in both position and voltage. The dip in mass growth seen just before the RH step is due to sudden changes in the flow system when turning on the humid flow after drying.

### 3 Results and Discussion

#### 3.1 Method validation for the retrieval of diffusivity coefficient of water

To validate our approach of diffusivity coefficient retrieval,  $D$  was determined for the same experiment shown in Fig. 6 using the numerical model described in detail in (Zobrist et al., 2011). The model treats the particle as consisting of up to several thousand individual shells and uses a composition and temperature dependent parametrization of the diffusion coefficient of water, simulating the growth and shrinkage of the particle resulting from water diffusion between the shells.

The model was driven by experimental RH(t) data while drying from 28% to 6% and then humidifying up to 28% as well as the initial radius. For the input, several parametrizations for the water activity dependent diffusivity were tested (see Fig. 7). Parametrization for every input  $D$  was derived by linear extrapolation of diffusivity in pure water ( $2 \times 10^{-5} \text{ cm}^2 \text{ s}^{-1}$ ) and input  $D$  at  $a_w = 0.17$  (ranging from  $1 \times 10^{-12} \text{ cm}^2 \text{ s}^{-1}$  to  $1 \times 10^{-11} \text{ cm}^2 \text{ s}^{-1}$ ), assuming that the  $a_w$  dependence of  $D$  is linear on a log scale.

As shown in Fig. 7, considerable agreement between experimental and modelled radius data is obtained when the input  $D$  was set between  $3 \times 10^{-12} \text{ cm}^2 \text{ s}^{-1}$  and  $8 \times 10^{-12} \text{ cm}^2 \text{ s}^{-1}$ .  $D$  derived for the same particle using the linear response approximation (fitting according to Eq. (4)) is  $3 \times 10^{-12} \text{ cm}^2 \text{ s}^{-1}$ . In addition, it can be clearly seen that while in the drying part the radius data retrieved from the model for the input  $D = 3 \times 10^{-12} \text{ cm}^2 \text{ s}^{-1}$  does not agree well with the experimental data, it agrees quite well after the step increase in RH. This is consistent with  $D$  derived from the fitting ( $3 \times 10^{-12} \text{ cm}^2 \text{ s}^{-1}$ ), which is done in the same RH range, i.e. the step increase. Thus,  $D$  derived using the two different approaches agree within a factor of 2, which is chosen as the uncertainty range in our determination of  $D$ .

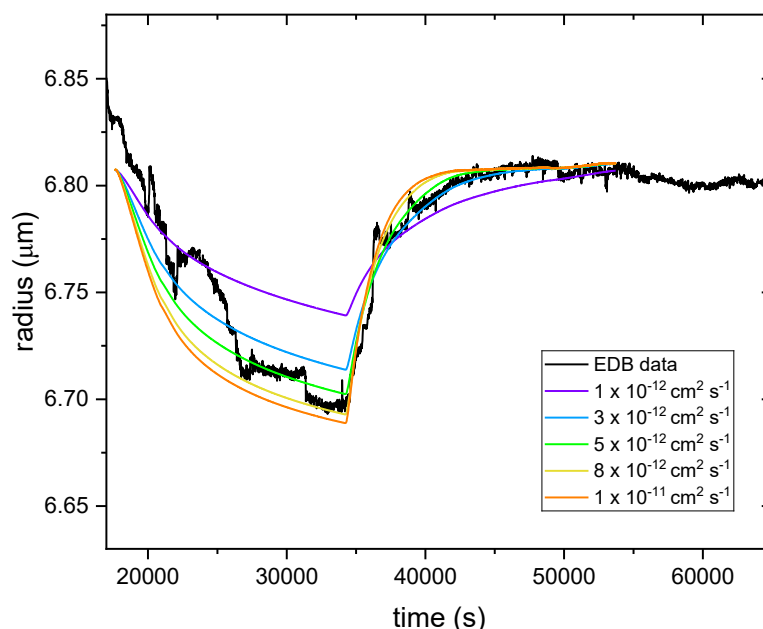


**Figure 7:** Radius data retrieved from the numerical model for different input  $D(a_w)$  (colored lines) in the range of  $1 \times 10^{-12} \text{ cm}^2 \text{ s}^{-1}$  (violet line) to  $1 \times 10^{-11} \text{ cm}^2 \text{ s}^{-1}$  (orange line) for  $D(a_w = 0.17)$  in comparison to the experimental radius data (black line) for AA particle subjected to a rapid increase in RH after aging with UV and  $\text{O}_3$  until 60% mass loss. Note: in the modeled data, the initial radius at RH 28% (for all input  $D$ ) is slightly lower than the equilibrium radius at the same RH after the step increase. This is because of the uncertainty in size data, as described in Appendix A.

### 3.2 Kinetics: comparison between ozonolysis and photolysis

Figure 8 shows the normalized mass remaining calculated from the voltage data compensating for the gravitational force as shown in Fig. 4. The mass of an aqueous AA particle remains constant in the absence of UV irradiation at 375 nm or  $\text{O}_3$  exposure, indicating that AA has a low vapor pressure and does not undergo any reaction in the presence of oxygen. In the presence of UV irradiation and/or  $\text{O}_3$  exposure, mass loss is observed, which is evidence for the occurrence of fragmentation reactions that eventually lead to the formation of volatile products that partition from the particle phase to the gas phase. Fragmentation reactions are known to be an important pathway for organic aerosol particles undergoing photochemical reactions as well as for particles exposed to oxidants (Dou et al., 2021; Kroll et al., 2015; Sun and Smith, 2024; O'brien and Kroll, 2019). However, as shown in Fig. 8, only slight mass loss is observed when photolysis is done under a nitrogen gas phase, highlighting the importance of oxygen in the photolysis mechanism. Acceleration in mass loss during photolysis of SOA when transitioning from nitrogen to zero air was also observed previously in a different study (Sun and Smith, 2024).

The decay kinetics of an AA particle upon reaction with ozone is linear with time, similar to a previous study (Willis and Wilson, 2022), which indicates that the ozonolysis reaction follows a zeroth-order kinetics. The slow kinetics observed for ozonolysis may be due to the conjugated structure of AA, which stabilizes the  $\text{C}=\text{C}$  double bond. According to the study by Willis and Wilson (2022), most of the reactions between  $\text{O}_3$  and AA occur in the particle bulk due to the slow reaction of AA with  $\text{O}_3$  and AA's low surface affinity.

In contrast to ozonolysis, the shape of the photolysis decay kinetics is not linear. It is slow in the beginning, then speeds up possibly due to the formation of more photoreactive intermediates or due to the initiation of an autocatalytic process. After about 60% mass loss, the reaction slows down again, most likely because most

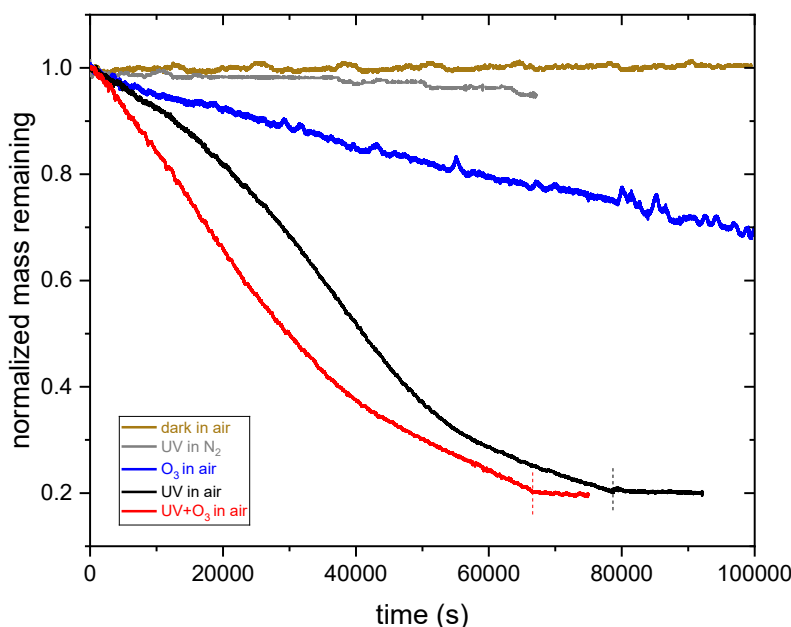


301 photoreactive species are consumed and non-absorbing products are formed or because of radical recombination.  
302 We conclude that similar to the findings by (O'Brien and Kroll, 2019) and (Sun and Smith, 2024), initial photolytic  
303 mass loss cannot be extrapolated to the entire SOA mass loss and that a photo-recalcitrant fraction remains, which  
304 prevents or slows down further mass loss.

305 Moreover, it can be inferred from Fig. 8 that the rate of decay of AA is slightly faster when photolysis is done in  
306 the presence of  $O_3$ . Since ozone is a stronger oxidant compared to oxygen, it might result in a faster mass loss,  
307 especially in the beginning of the reaction, where the oxidant is most likely the limiting factor. After the initial  
308 induction period, the rates of both reactions become comparable because of the occurrence of acceleration in the  
309 absence of  $O_3$ .

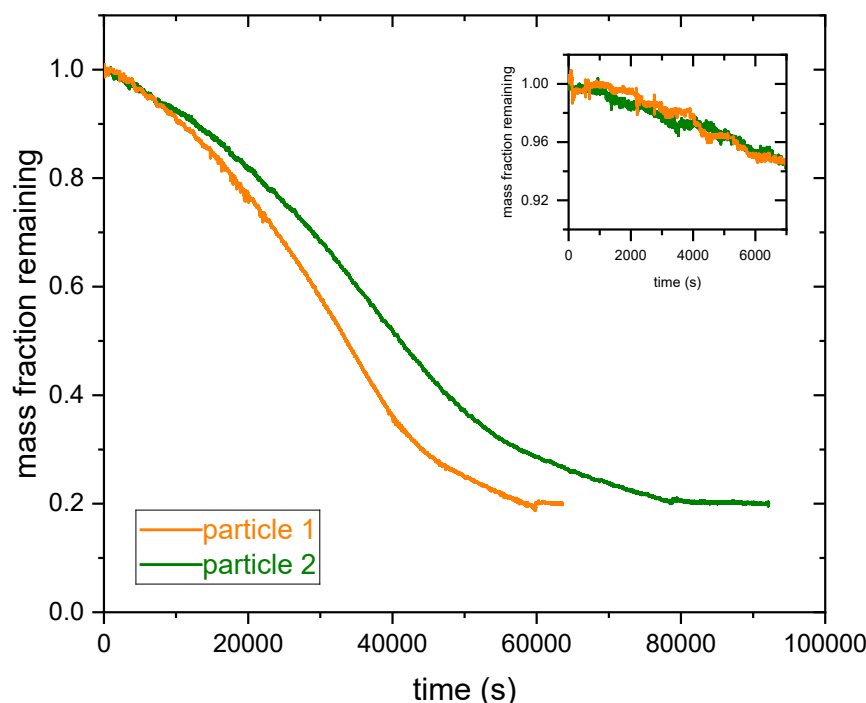
310 Additionally, regarding the photolysis experiments, it can be inferred from Fig. 9 that the rates of reaction of two  
311 different AA particles with UV irradiation overlap in the beginning of the experiment, but acceleration in mass  
312 loss of particle 1 occurs before particle 2. For instance, after an exposure time of 40,000 s, particle 1 lost 64% of  
313 its mass whereas particle 2 lost 48% (see Fig. 9). This is most likely because oxygen is the rate limiting factor in  
314 the beginning of the reaction. As the reaction proceeds, the intensity of the UV irradiation becomes important,  
315 which results in different reaction rates. This might be due to slightly different particle sizes and the position of  
316 the particle relative to the laser beam, which can affect the photon flux into the particle and thus the reaction rate.  
317 For this reason, mass loss was used instead of exposure time to represent the extent of aging, as will be presented  
318 in the following sections. However, mass loss and exposure time are well correlated (see Fig. E-1 in the appendix),  
319 but mass loss was chosen to account for the differences between different particles in terms of the reaction rate,  
320 assuming that at a certain mass loss, rather than exposure time, different particles should have similar chemical  
321 composition despite having different reaction rates.

322



323

324 **Figure 8: Comparison of the decay kinetics of an AA particle exposed to 375 nm UV irradiation in pure nitrogen and in**  
325 **synthetic air, 10 ppm  $O_3$  in synthetic air, and UV+ $O_3$  in synthetic air. Vertical dashed lines correspond to switching off**  
326 **UV (black) and UV+ $O_3$  (red).**



327

328 **Figure 9: Comparison of the decay kinetics between two different AA particles exposed to 375 nm UV irradiation until**  
 329 **80% mass loss. The inset graph shows the first 7,000 s to emphasize the overlap in the initial reaction rate between the**  
 330 **two experiments.**

331

### 332 3.3 Phase separation during ozonolysis

333 Figure 10 shows the mean fringe distance (a) and pattern distortion parameter (b) of a 532 nm laser-illuminated  
 334 AA particle upon exposure to ozone. After about an hour of O<sub>3</sub> exposure, the TAOS pattern of the particle becomes  
 335 irregular and the pattern distortion parameter, which denotes the asymmetry in the scattering pattern (Braun and  
 336 Krieger, 2001), becomes larger. This indicates that the particle is no longer homogenous and spherical and has lost  
 337 its symmetry, resulting in light scattering with different intensities depending on its orientation relative to the laser  
 338 beam. This behavior was observed only upon exposure to O<sub>3</sub> and was confirmed through five other O<sub>3</sub> exposure  
 339 experiments, where an irregularity in the TAOS pattern was observed for all particles after an exposure time of 65  
 340 ± 8 min. On the contrary, AA particles exposed to UV illumination or UV and O<sub>3</sub> simultaneously remained  
 341 spherical symmetric upon aging. The observed heterogeneity in the particle upon ozonolysis could be due to liquid-  
 342 liquid phase separation (LLPS) exhibiting partial wetting morphology. Similar behavior was observed in other  
 343 studies upon ozonolysis of oleic acid particles (Hosny et al., 2016) and squalene droplets (Athanasiadis et al.,  
 344 2016). However, in the case of ozonolysis of oleic acid, they observed a wide range of species: small oxidized  
 345 polar molecules and large non-polar oligomers, which are immiscible and can favor LLPS. Here, we did not  
 346 perform chemical characterization of the ozonolysis products, but (Willis and Wilson, 2022) identified products  
 347 having two to seven carbon atoms with different carbon oxidation states (~1 to 3) in AA ozonolysis experiments.  
 348 It might be possible that some of the small products with high carbon oxidation state are immiscible with the larger  
 349 products with low oxidation state, which can cause phase separation. Another possibility for the observed  
 350 symmetry loss in light scattering would be precipitation of *trans*-aconitic acid or one of the ozonolysis products  
 351 that is insoluble in water, creating two phases: solid precipitate and dissolved liquid phase, since the particles  
 352 contain significant amount of water as they are kept at relatively high RH (above 78%).

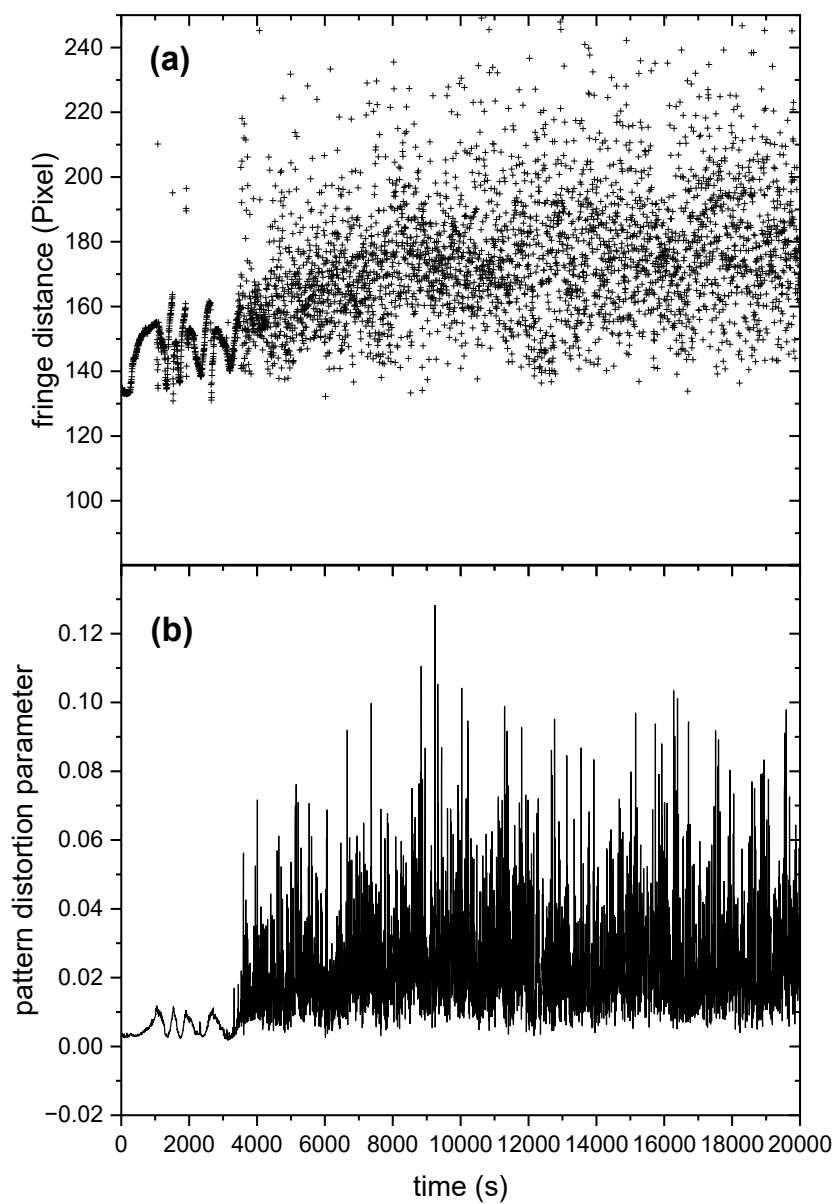




**Figure 10: (a) Mean fringe distance and (b) pattern distortion parameter of 532 nm laser-illuminated AA exposed to O<sub>3</sub>. Only the data for the first 20,000 s are plotted here to present clearly the phase transition occurring at ~3,500 s, indicated by the significant increase in fluctuations in fringe distance (a) and pattern distortion parameter (b).**

### 3.4 Phase state of AA after aging

In contrast to untreated AA, which effloresced typically at RH 59.9%, AA particles aged with UV or UV and O<sub>3</sub> simultaneously did not crystallize upon drying. This was deduced from the TAOS pattern, which remained regular upon drying, implying that the aged particles remained liquid or amorphous solid, but not crystalline. After AA particles undergo chemical reaction, a mixture of products is produced, which makes efflorescence less likely to occur due to thermodynamic reasons.

Similar behavior in terms of suppression or inhibition of efflorescence after aging was observed previously. For instance, suppression of crystallization was observed upon ozonolysis of mixed maleic acid/ammonium sulfate particles and subsequent drying (Chan and Chan, 2012). In another study, maleic acid particles exposed to O<sub>3</sub> showed efflorescence at lower RH compared to unprocessed maleic acid particles, with some particles not efflorescing at any RH (Pope et al., 2010).

Furthermore, for AA particles aged with UV or UV and O<sub>3</sub> only up to 20% or 26% mass loss, although the particles remained spherical upon drying, the TAOS pattern became irregular after RH was increased rapidly from 6% to 28%, indicating crystallization of AA (see Appendix F). This could be due to restructuring the hydrogen bonding network favoring nucleation. Alternatively, if nucleation already occurred during drying, the plasticizing effect of water could lead to crystal growth after water uptake. This behavior was not observed for particles that lost more than 25% of their mass because of the conversion of considerable amount of *trans*-aconitic acid into a mixture of products, which inhibited crystallization.

### 3.5 Viscosity and hygroscopicity of AA before aging

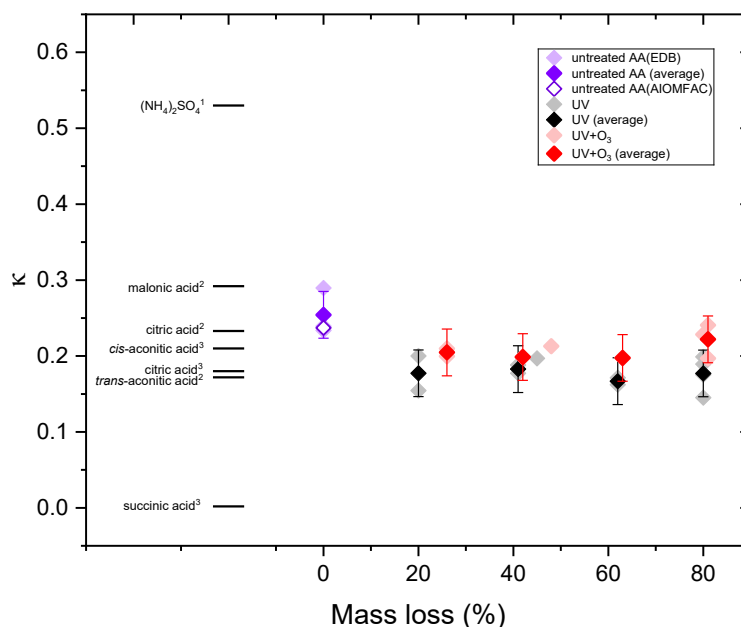
The average viscosity of untreated AA derived from our experiments at room temperature (~298K) and RH 17.7 ± 0.5% (midpoint of the step in RH 6–28%) is 1.2 × 10<sup>3</sup> Pa s. Aconitic acid and citric acid are structurally similar: both are tricarboxylic acids having 6 carbon atoms. (Song et al., 2016) measured the viscosity of citric acid by droplet coalescence at ambient temperature and reported as 5.1 × 10<sup>3</sup> Pa s at 18 % RH, which is within a factor of 4 of the viscosity of AA determined in this study. The slightly higher viscosity of citric acid compared to aconitic acid might be due to the additional hydroxyl group, which enhances hydrogen bonding (Rothfuss and Petters, 2017) and the lower temperature of the coalescence experiment.

Figure 11 shows the hygroscopicity results in terms of derived  $\kappa$  values. For reference, a selection of  $\kappa$  values of other organic acids are taken from the literature. As shown in this figure, organic acids can have quite different  $\kappa$  values. Higher  $\kappa$  values indicate higher hygroscopicity. Hygroscopicity of organic compounds depends on molecular structure and physicochemical properties. Organic compounds having more functional groups, such as carboxyl, carbonyl, and hydroxyl tend to be more hygroscopic (Han et al., 2022). In general, polar organic compounds having higher O:C are more hygroscopic (Han et al., 2022; Lambe et al., 2011; Duplissy et al., 2011). In addition, organic compounds that are more water soluble tend to be more hygroscopic because they would have a higher molar concentration in the saturated solution corresponding to a stronger reduction in water activity (Han et al., 2022).

Average  $\kappa$  of untreated AA measured in this study is 0.254 ± 0.031, which agrees within error with *cis*-aconitic acid (0.21) determined in another study (Han et al., 2022) and that predicted by AIOMFAC model (0.237) (Zuend et al., 2011; Zuend et al., 2008), but is significantly higher than that of *trans*-aconitic acid (0.172 ± 0.010) determined in another study (Rickards et al., 2013). In our study, fitting was done between RH 62% and 80%, which is different from the RH used in Rickards et. al (> 90%), which could be one reason for the difference. Variations in  $\kappa$  for the same organic acid between different studies have been observed previously. For instance, as shown in Fig. 11,  $\kappa$  for citric acid determined using a humidified tandem differential mobility analyzer (HTDMA) at RH 90% was found to be 0.18 (Han et al., 2022), while that determined using aerosol optical tweezers (AOT) at RH 66% was found to be 0.233 ± 0.035 (Rickards et al., 2013). In the following, we focus on changes in  $\kappa$  with aging rather than on absolute  $\kappa$  values.



404



405

406

407 **Figure 11: The hygroscopicity of AA particles before and after UV and UV+O<sub>3</sub> aging in comparison with (NH<sub>4</sub>)<sub>2</sub>SO<sub>4</sub>,  
 408 malonic acid, citric acid, cis-aconitic acid, trans-aconitic acid, and succinic acid data taken from the literature: (1)  
 409 (Petters and Kreidenweis, 2007) (2) (Rickards et al., 2013) (3) (Han et al., 2022).**

### 410 3.6 Viscosity and hygroscopicity of AA after aging

411 Figure 12 shows the viscosity of untreated AA and AA aged with UV and UV and O<sub>3</sub> simultaneously up to 20%,  
 412 40%, 50%, 60%, and 80% mass loss. All measurements were done at room temperature (~298 K) and at RH 17.7  
 413 ± 0.5%. The viscosity of AA exposed to UV and O<sub>3</sub> simultaneously increased with the extent of aging, with the  
 414 aged AA at 80% mass loss being almost 4 orders of magnitude higher compared to that of the untreated AA. UV  
 415 exposure alone also resulted in an increase in viscosity but only up to 60% mass loss. Surprisingly, further UV-  
 416 aging (80% mass loss) led to a reduction in viscosity. However, with UV-aging at 80% mass loss, there is a large  
 417 spread in the viscosity data, where some of the values at the lower viscosity range were beyond the limit of  
 418 determination with our method (see Appendix D). Since the discrepancies in the viscosity values are mainly  
 419 between size and mass measurement for the same particle, rather than being between different experiments, the  
 420 uncertainty is most likely due to experimental error at 80% mass loss, where the particle becomes small, increasing  
 421 the error on both size and mass measurements. Thus, it is difficult to conclude the exact viscosity at 80% mass  
 422 loss, but it is evident that the viscosity in all cases is significantly less than the one at 60% mass loss.

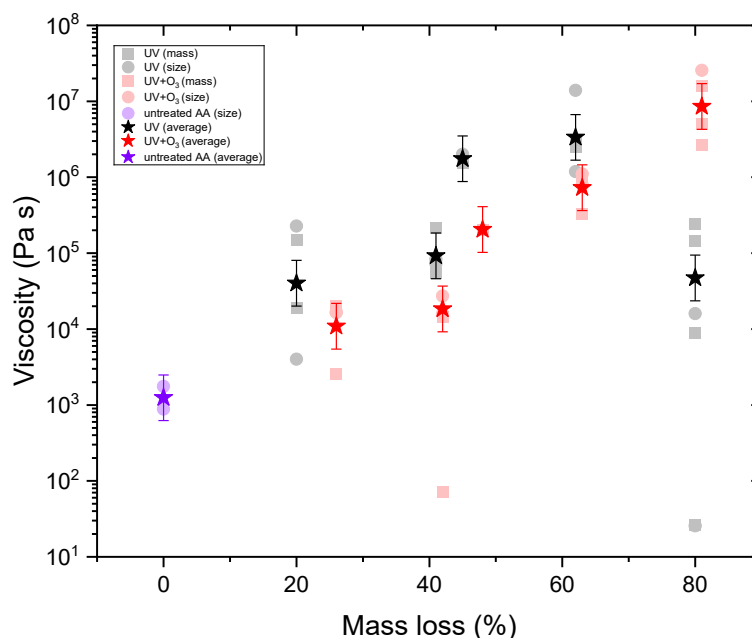


**Figure 12: The viscosity of AA particles before and after UV and UV+O<sub>3</sub> aging from mass and/or size data.**

As shown in Fig. 11, average  $\kappa$  of aqueous AA particles decreased slightly from  $0.254 \pm 0.031$  to  $0.177 \pm 0.031$  upon aging with UV light till 20% mass loss. Upon further aging,  $\kappa$  remained almost constant. For the AA particles aged with UV and O<sub>3</sub> simultaneously, less significant reduction in  $\kappa$  was observed. Similar to UV-aging,  $\kappa$  decreased from  $0.254 \pm 0.031$  to  $0.205 \pm 0.031$  after 25% mass loss, but then it remained almost constant with further aging. However, this reduction is not significant, taking the uncertainty in  $\kappa$  into account. In addition, overall  $\kappa$  values for UV+O<sub>3</sub> aged AA are a bit higher than those of UV-aged AA, consistent with the viscosity values, which show slightly lower viscosity for UV+O<sub>3</sub> aged AA up to 60% mass loss.

Currently, we do not have any information about the chemical composition of the particles after aging. However, we may draw some conclusions from the data shown in Fig. 11 and 12. Since hygroscopicity did not increase after aging, O:C is also expected to remain almost constant or decrease slightly after aging. While it is known that hygroscopicity and carbon oxidation state increase after oxidative aging (Jimenez et al., 2009; Kroll et al., 2011; Kroll et al., 2015), no significant or small net change in O:C was observed after photolysis of SOA in other studies (Romonosky et al., 2015; O'brien and Kroll, 2019). It should be noted that in this study, only the hygroscopicity and viscosity of the condensed phase after aging are measured, without considering the highly volatile compounds evaporating to the gas phase. It is still expected that the overall carbon oxidation state increased after aging in our study if the compounds lost to the gas phase are also considered. As gas phase oxidants are involved in the aging process (O<sub>2</sub> in UV-aging and O<sub>3</sub> in UV+O<sub>3</sub> aging), it is expected that polar oxygen containing functional groups are added after oxidation. Since these groups weaken adjacent C-C bonds, fragmentation reactions will take place, leading to volatilization of smaller fragments to the gas phase. This mechanism can be indirectly inferred from Fig. 8, where initially an induction period appears, followed by rapid mass loss. However, it is expected that the most highly oxidized carbon will exist mainly in the gas phase (Kroll et al., 2011). Therefore, although the small, fragmented products are expected to have higher oxidation state, they are also expected to be volatile, thus the oxidation state of the particle can decrease slightly after these fragments evaporate (O'brien and Kroll, 2019; Hildebrandt Ruiz et al., 2015). However, we cannot prove that O:C remained constant or decreased slightly, since





we did not determine the chemical composition of the products. Note that if O:C increased after aging, but if the average molecular weight increased as well, the hygroscopicity may still decrease.

Viscosity increase upon SOA aging was observed previously in the UV-aging of d-limonene and  $\alpha$ -pinene SOA (Baboomian et al., 2022). Mass spectrometric analysis indicated that the increase in d-limonene SOA viscosity was most likely due to changes in the chemical properties because an average increase in molecular weight, elemental O:C ratio, number of carbon atoms per molecule, and double bond equivalent was observed (Baboomian et al., 2022). However, in contrast to our study, photolysis of SOA was done at low RH. Water content of the particle during photolysis can play an important role in the mechanism of formation of products and thus in the viscosity of the final products. For instance, when photolysis of SOA was performed in aqueous solution instead of low RH, reduction in carbon number was observed, which was attributed to the degradation of dimers and trimers (Romonosky et al., 2015). Another study comparing condensed-phase SOA photolysis at low RH and aqueous photolysis found that the signal intensity obtained by mass spectrometry in the larger m/z range remained similar before and after exposure, while lower m/z range was higher after aqueous photolysis, but lower after condensed-phase photolysis (Sun and Smith, 2024). They attributed this difference to the evaporation of the volatile products from the condensed phase, but retention of these species in the aqueous solution. Direct comparison of our study to these studies is difficult, since in our case condensed-phase photolysis was done at higher RH. However, since mass loss was observed and the viscosity increased after UV-aging, it can be inferred that the smaller volatile fragments evaporated, leaving relatively larger non-volatile products in the particle.

One possible explanation for the observed viscosity enhancement after aging is the formation of oligomers from product fragments. Oligomers, due to their high molecular weight, could contribute to increased viscosity. However, the formation of oligomers might be hindered under the experimental conditions, as the reactions occur at moderately high RH, and the presence of water typically slows down oligomerization. It is important to note, though, that the particles are more concentrated in water at these RH levels (even at 85%) compared to typical aqueous-phase chemistry, which may facilitate oligomer formation. Additionally, oligomerization could have occurred during the drying process just before viscosity measurements were taken.

Alternatively, the increase in viscosity could be attributed to changes in the hydrogen bonding network. The intermolecular hydrogen bonding between the products might be enhanced compared to untreated AA, leading to a higher viscosity. Further UV-aging could degrade some of these products or the oligomers, potentially altering the hydrogen bonding interactions and causing a decrease in viscosity upon continued aging.

The continuous increase in viscosity upon aging with UV and O<sub>3</sub> simultaneously until 80% mass loss suggests that the aging mechanism and the products formed are different in the presence of oxidants like O<sub>3</sub>. The presence of O<sub>3</sub> might favor the formation of oligomers, therefore increasing the viscosity of the particles further with longer exposure.

#### 4 Conclusion

In this study, the viscosity and hygroscopicity of aqueous *trans* aconitic acid particles were determined after exposure to 375 nm UV irradiation or UV irradiation and O<sub>3</sub>. Photolysis and ozonolysis resulted in significant mass loss because of fragmentation reactions followed by volatilization and displayed different reaction kinetics. Ozonolysis alone disrupted the light scattering symmetry of the particle, indicating a phase transition. Aging with UV or UV and O<sub>3</sub> resulted in the inhibition of efflorescence upon drying. The viscosity of the particles increased by almost 4 orders of magnitude upon aging with UV and O<sub>3</sub> simultaneously. UV-aging also resulted in an increase in viscosity but only up to 60% mass loss. Further UV-aging resulted in a reduction in viscosity. Hygroscopicity of the particles decreased slightly after exposure to UV laser up to 20% mass loss and then stayed constant with further aging. A similar trend, though less significant, was observed for combined UV and O<sub>3</sub> aging.

To check the relevance of our study to atmospheric conditions, we estimated the characteristic mixing times within the particles after aging. The increase in viscosity upon aging implies for particles with a radius of 100 nm (typical of accumulation mode SOA particles) a characteristic mixing time of 4 h compared to 4 s for the unexposed particles under dry boundary layer conditions. For colder temperatures in the free troposphere, the mixing times could be still longer even at higher relative humidity.

Therefore, the changes in viscosity, hygroscopicity, phase state, volatility, and mixing times observed in this study provide further evidence on how aging can directly alter the physicochemical properties of aerosol particles, with



501 indirect consequences on climate and human health. Our results show that the presence of gas phase oxidants like  
502 ozone, in addition to UV light, results in viscosity enhancement, an effect seen previously in the UV-aging of SOA.  
503 This viscosity enhancement is most likely due to the formation of oligomers of high molecular weight. However,  
504 from the shape of reaction kinetics, hygroscopicity, and viscosity results, we conclude that the mechanism of aging  
505 is different in the presence of gas phase oxidants compared to photochemical aging without gas phase oxidants.  
506 To understand better the mechanism behind the differences that we observe, we plan to study in the future the  
507 chemical composition of the products during aging using mass spectrometry.

508

509

510

511

512

513

514

515

516

517

518

519

520

521

522

523

524

525

526

527

528

529

530

531

532

533

534

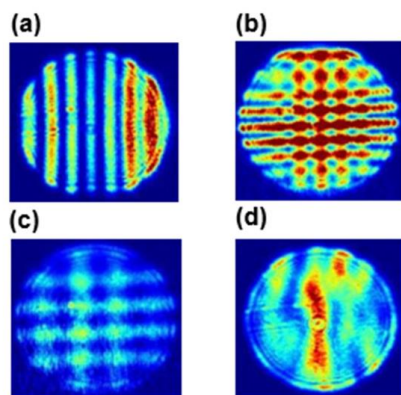
535

536

537



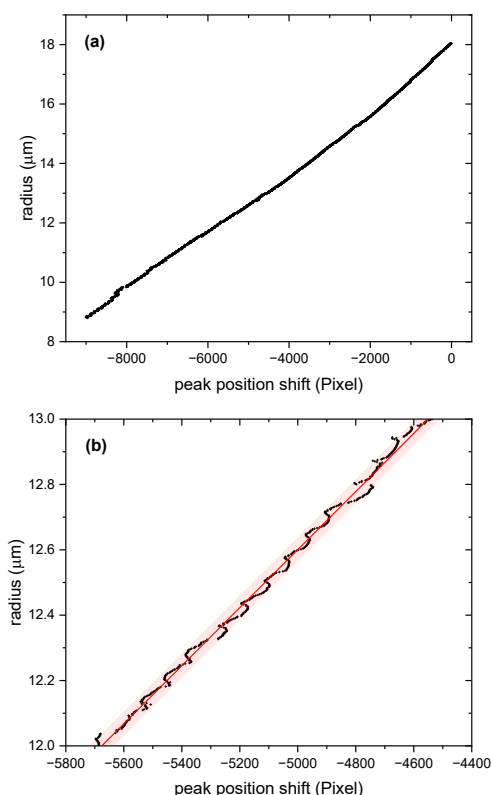
538 **Appendix A. Size retrieval from two-dimensional angular optical scattering (TAOS) pattern**  
 539 The EDB configuration and geometrical constraints allow us to measure the TAOS pattern within about  $5^\circ$  half  
 540 apex angle around  $100^\circ$  scattering. Figure A-1 shows four TAOS-patterns observed in our experiments.



541  
 542 **Figure A-1: (a) TAOS pattern of a spherical symmetric trans-aconitic acid particle upon illumination with polarized**  
 543 **532 nm laser, fringe intensity is rainbow color coded in arbitrary units. (b) pattern of a particle upon illumination by**  
 544 **both the polarized 532 nm laser and the orthogonally polarized 375 nm laser. (c) same as (b) but after photochemical**  
 545 **aging. (d) TAOS pattern for 532 nm illumination only after phase transition induced by ozonolysis.**

546 Comparing Fig. A-1(d) with the other panels of Fig. A-1 illustrate that the regular TAOS pattern is distorted once  
 547 the spherical symmetry of a particle is lost. In comparison to Fig. A-1(b), the average fringe distance for both  
 548 orthogonal fringe patterns in Fig. A-1(c) has increased, indicating shrinkage during aging. Quantitative analysis of  
 549 these types of patterns, i.e. size retrieval, has been discussed extensively in the literature (Davis and Periasamy,  
 550 1985; Steiner et al., 1999; Jakubczyk et al., 2013; Davies, 2019). A fast, simple method for sizing a spherical  
 551 symmetric particle is based on scattered light angular frequency determination (Steiner et al., 1999), which requires  
 552 a calibration of the TAOS pattern in terms of scattering angle. We follow the suggestion by (Davies, 2019) and  
 553 measure the evaporation rate of a pure compound for calibration, here PEG-4 for which the vapor pressure is well  
 554 established (Krieger et al., 2018).

555 Sizing by measuring the characteristic angular frequency works best for scattering angles smaller than  $60^\circ$ .  
 556 However, our scattering angle is  $100^\circ$  and our apex angle is quite small due to spatial restriction in our setup. This  
 557 limits its applicability to small size changes, as the uncertainty in sizing using the characteristic angular frequency  
 558 is of the order of  $\pm 1 \mu\text{m}$  for our scattering geometry and typical particle size. Therefore, for measuring small size  
 559 changes, we apply a method based on spectral shift of Mie-resonance spectra (Zardini et al., 2006) to angular shift  
 560 of a peak position in the TAOS pattern. Compare this approach with a related method based on tabulated peak  
 561 positions suggested by (Davies, 2019). Figure A-2 shows data taken for an evaporating PEG-4 particle at constant  
 562 temperature. Panel (a) shows that the radius scales almost linearly over a wide size range with the total peak  
 563 position shift in the TAOS pattern. On closer inspection (see panel (b) of Fig. A-2), the relationship is irregular on  
 564 small scales but allows the reliable detection of size changes of about  $\pm 40 \text{ nm}$ . In our application, we are focusing  
 565 on characteristic time scales of small size changes due to rapid changes in relative humidity: there, the irregularity  
 566 between size and peak position shift for small size changes influences the determination of characteristic time only  
 567 slightly (see Fig. 6 in main text.)



568

569 **Figure A-2: (a)** Size data of an evaporation experiment (PEG-4 at 24°C) versus peak position shift. Evaporation rate  
 570 was calculated from known data of vapor pressure (Krieger et al., 2018) and radius was determined through comparison  
 571 of measured characteristic angular frequency with evaporation rate. **(b)** Zoom into the data of (a) showing that radius  
 572 can be measured with a sensitivity of about  $\pm 40$  nm when measuring the peak position shift. Note however, that the  
 573 relationship between peak position shift and size is not strictly linear, but irregular within a size change of approximately  
 574 40 nm.

575

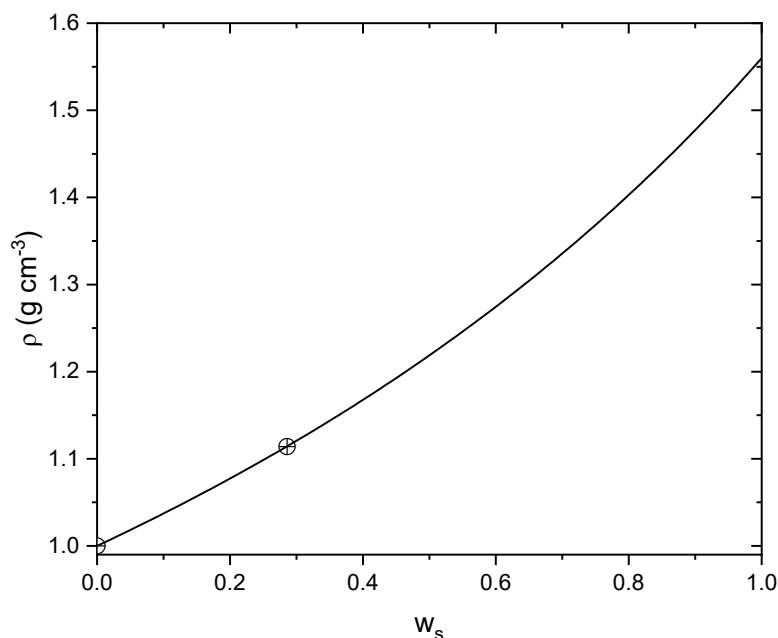
## 576 **Appendix B. Density determination of aqueous AA**

577 To determine the density of aqueous AA under dry conditions ( $\rho_0$ ), the density of AA at mass fraction  $w_s = 0.286$   
 578 was measured using a pycnometer. Assuming the conventional additivity rule holds (Lienhard et al., 2012; Steimer  
 579 et al., 2015):

$$580 \quad \rho(w_s) = \left( \frac{1-w_s}{\rho_w} + \frac{w_s}{\rho_0} \right) \quad (B1)$$

581 where  $\rho(w_s)$  is the density of solute at mass fraction  $w_s$ ,  $\rho_w$  is the density of water, we retrieve  $\rho_0$ , the density of  
 582 aqueous AA solute at dry conditions, i.e. the subcooled melt density. Based on the known density of water and our  
 583 measured density at  $w_s = 0.286$ ,  $\rho_0 = 1.56 \text{ g cm}^{-3}$ .

584



585

586 **Figure B-1: Density ( $\rho$ ) vs. mass fraction ( $w_s$ ) parametrization for aqueous AA according to Eq. (B1).**

587

588 **Appendix C.** Deconvolution of linear response to an exponential ‘step’ in relative humidity, derivation of Eq. (4)

589 Let’s assume the dynamic system is a linear time-invariant one, with the response of the system to a step input  
 590 (Heaviside function,  $H(t)$ ) is given by:

591 
$$y(t) = 1 - e^{-k_1 t}$$

592 Now, instead of a step input,  $H(t)$ , the input function is given by:

593 
$$RH(t) = 1 - e^{-k_2 t}$$

594 In our experiment, we obtain  $k_2$  by analyzing the data  $RH(t)$ , with  $k_2$  being the rate constant of the RH-step. We  
 595 want to determine the system’s response  $y(t)$  to the input  $RH(t)$ . Very generally, the system’s response is given  
 596 by the convolution integral:

597 
$$y(t) = \int_0^t RH(\tau) h(t - \tau) d\tau$$

598 where the impulse response  $h(t)$  is the derivative of the system to a step response  $H(t)$ :

599 
$$h(t) = k_1 e^{-k_1 t}, \quad t > 0$$

600 For the step response,  $H(t)$ , the radius or mass evolution is related to the impulse response by:

601 
$$y(t) = \int_0^t h(\tau) d\tau$$

602 Therefore, substituting the RH input function and the impulse response function by



603  $h(t - \tau) = k_1 e^{-k_1(t-\tau)}$ , we get:

604 
$$y(t) = \int_0^t (1 - e^{-k_2(\tau)}) k_1 e^{-k_1(t-\tau)} d\tau$$

605 Expanding the integral:

606 
$$y(t) = k_1 e^{-k_1 t} \int_0^t (1 - e^{-k_2 \tau}) e^{k_1 \tau} d\tau$$

607 Solving the integral leads to the final expression for  $y(t)$ :

608 
$$y(t) = (1 - e^{-k_1 t}) - \frac{k_1}{k_1 - k_2} (e^{-k_2 t} - e^{-k_1 t})$$

609 Replacing the rate constants with their inverse, i.e. the characteristic time constants  $\tau_1 = 1/k_1$  and  $\tau_2 = 1/k_2$ ,  
 610 yields Eq. (4):

611 
$$y(t) = (1 - e^{-t/\tau_1}) - \frac{\tau_2}{\tau_2 - \tau_1} (e^{-t/\tau_2} - e^{-t/\tau_1})$$

612

613 **Appendix D.** Comparing the linear response approximation of Appendix C to a numerical model solving the  
 614 diffusion equation

615 As noted in the main text, the linear response approximation for water uptake kinetics is expected to diverge from  
 616 the full solution of Fick's second law when water diffusivity becomes sufficiently slow. Here, we compare the size  
 617 change resulting from water uptake under an ideal exponential 'step'-like change in RH, using a numerical model  
 618 based on the Euler forward method to solve the diffusion equation (Zobrist et al., 2011), with the linear  
 619 approximation described in Appendix C.

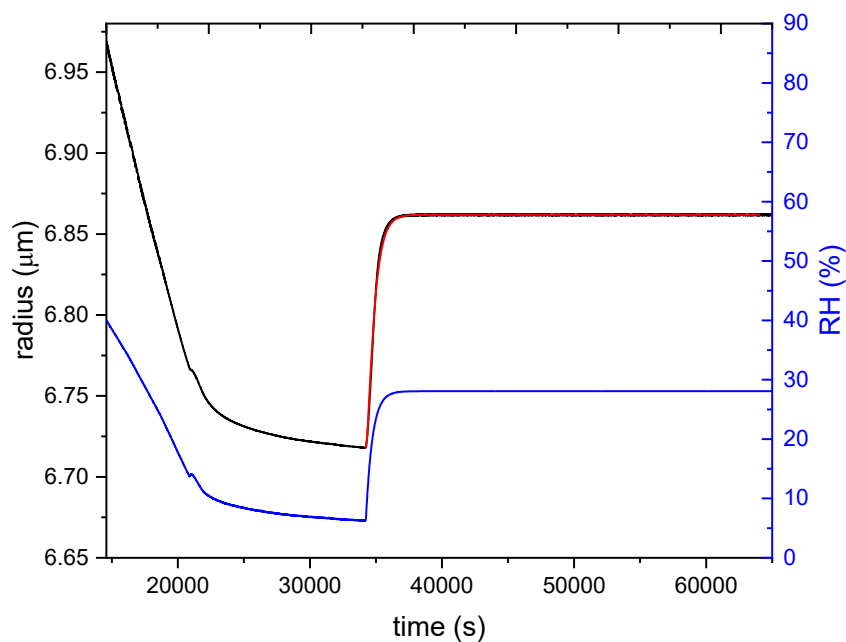
620 Since we use the same flow changes in all our experiments and the particle sizes in the experiments vary only over  
 621 a rather small size range, we can restrict the comparison to an idealized  $RH(t)$  pathway taken from our  
 622 experimental observations as well as choosing a particular initial radius. Figure D-1 shows the  $RH(t)$  pathway  
 623 chosen as a blue line, the size response predicted by the numerical model as a black line and a linear regression of  
 624 Eq. (4) to the size predicted by the numerical model as a red line. For simplicity, we assume as input for the  
 625 numerical model that the dependence of water diffusivity on water activity follows an exponential dependence for  
 626 water activities with the water diffusivity for pure water fixed to  $2 \times 10^{-5} \text{ cm}^2 \text{ s}^{-1}$ . At 40% RH, an initial radius of  
 627  $6.969 \mu\text{m}$  is set and it is assumed that at this starting RH before drying the particle is internally mixed in water  
 628 content. For the simulation of Fig. D-1, we set the water diffusivity  $D$  ( $a_w = 0.17$ ) to  $2 \times 10^{-10} \text{ cm}^2 \text{ s}^{-1}$ . As evident  
 629 from Fig. D-1 for these parameters, the linear approximation seems to mirror the predictions of the numerical  
 630 model very well.

631 Following this approach, we test the linear response for the range of  $D$  ( $a_w = 0.17$ ) between  $5 \times 10^{-13} \text{ cm}^2 \text{ s}^{-1}$  to  $2 \times$   
 632  $10^{-7} \text{ cm}^2 \text{ s}^{-1}$ . Some of the results are shown in Fig. D-2. It becomes clear that our experiments are not sensitive to  
 633  $D$  (at  $a_w = 0.17$ )  $> 2 \times 10^{-9} \text{ cm}^2 \text{ s}^{-1}$ , simply because our experimental setup yields a rather slow response in  $RH(t)$   
 634 upon a step change in gas mass flows (We cannot increase the total flow much beyond 50 sccm to allow mass  
 635 measurements). For this reason, the second step increase in RH (from 28% to 49%), shown in Fig. 4 in the main  
 636 text, was not evaluated. Figure D-2 shows in addition the expected deviation from linear response with low water  
 637 diffusivities (panels e and f).

638 However, we can correct for the differences between numerical model and linear approximation for a limited range  
 639 of water diffusivities as shown in Fig. D-3. There, we compare the characteristic time constant,  $\tau_1$ , obtained from  
 640 the linear regression to Eq. (4) to the input parameters of the numerical model represented as characteristic time  
 641 according to Eq. (5). Perfect agreement between both is indicated as the dashed line. The limited range of  
 642 characteristic response times for which the linear approximation works is clearly visible from Fig. D-3. It allows  
 643 us to deduce an empirical correction factor which we apply for characteristic response times measured in our  
 644 experiments ranging from 20 s to about 27,000 s. Fortunately, this is approximately the time range we do observe  
 645 in our experiments for untreated AA and the most viscous aged particles.

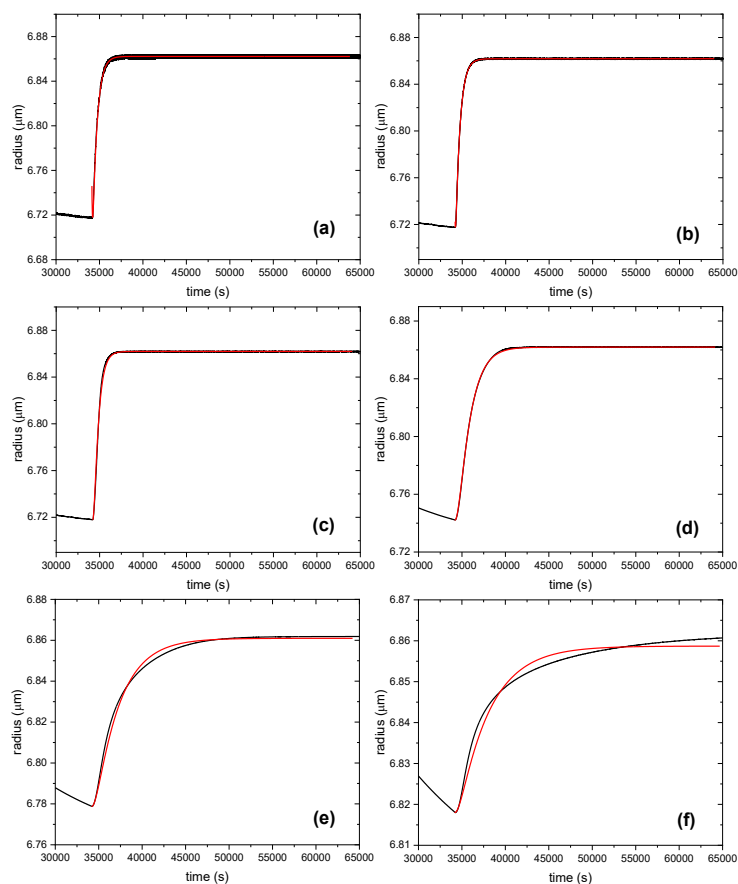


646



647

648 **Figure D-1: The blue line represents the RH data. The black line represents the radius data obtained from the numerical**  
 649 **model for an input  $D$  of  $2 \times 10^{-10} \text{ cm}^2 \text{ s}^{-1}$ . The red line is the first-order kinetics fitting according to Eq. (4) on the size**  
 650 **response data after increasing RH rapidly.**



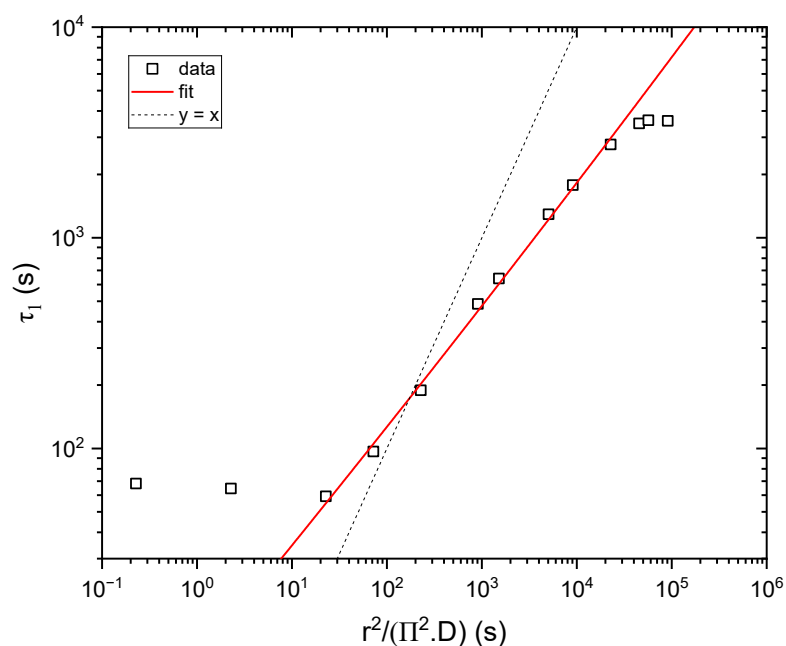
651

652 **Figure D-2: The black line represents the size data obtained from the numerical model for an input D (at  $a_w = 0.17$ ) of**  
 653 **(a)  $2 \times 10^{-8} \text{ cm}^2 \text{ s}^{-1}$ , (b)  $2 \times 10^{-9} \text{ cm}^2 \text{ s}^{-1}$ , (c)  $2 \times 10^{-10} \text{ cm}^2 \text{ s}^{-1}$ , (d)  $9 \times 10^{-12} \text{ cm}^2 \text{ s}^{-1}$ , (e)  $2 \times 10^{-12} \text{ cm}^2 \text{ s}^{-1}$ , and (f)  $5 \times 10^{-13} \text{ cm}^2 \text{ s}^{-1}$ . The red line shows the linear response approximation regression curve.**  
 654

655

656





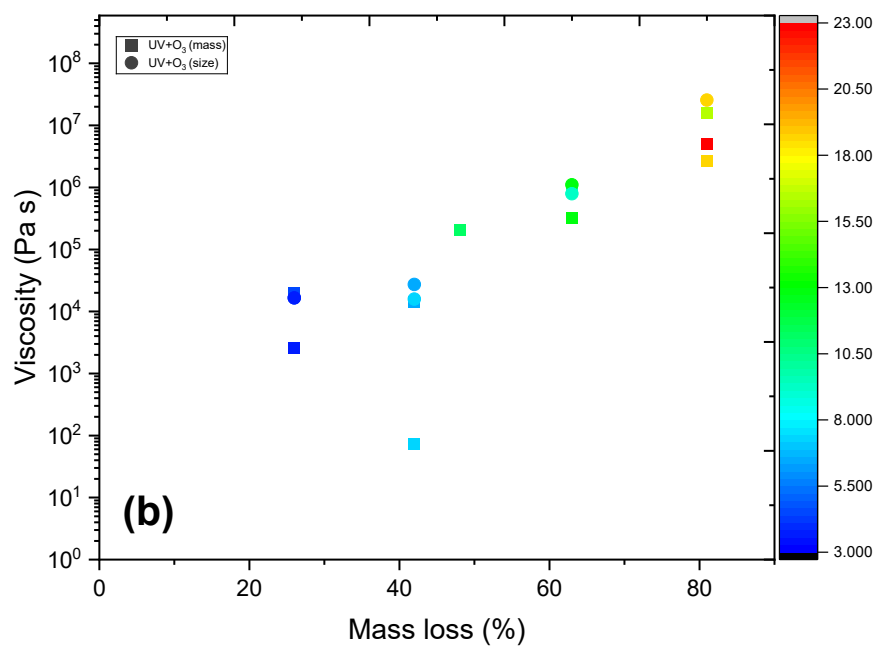
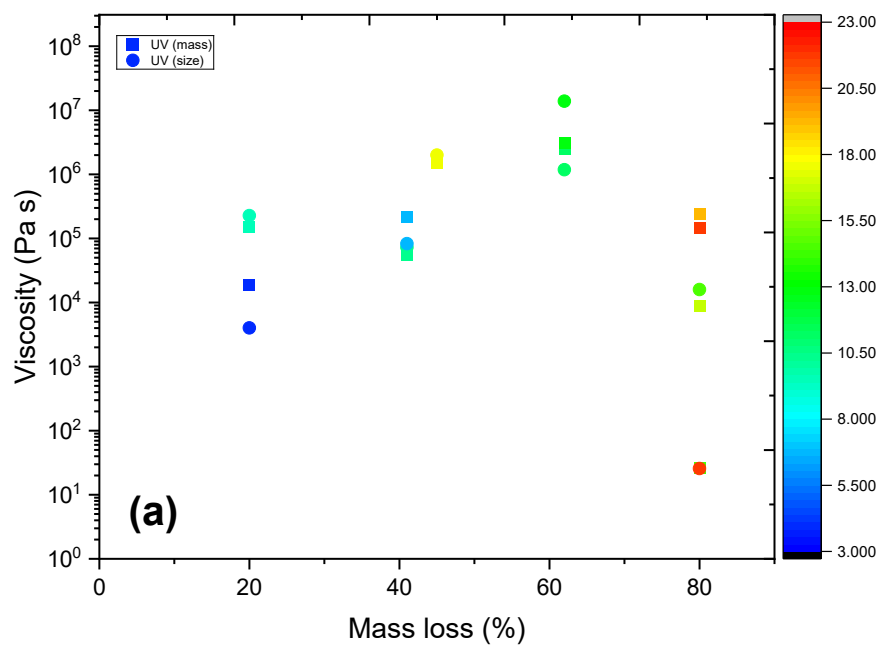
657

658 **Figure D-3: Output  $\tau_1$  data determined using the exponential function vs. input  $r^2/(\Pi^2.D)$  data determined using the**  
 659 **numerical model. The red line represents the fit on the output vs. input data. The dashed line shows  $\tau_1 = \frac{r^2}{\Pi^2.D}$ .**

660

661 **Appendix E. Correlation between mass loss and exposure time**

662 Figure E-1 shows that as mass loss increases, exposure time also increases for both UV and UV+O<sub>3</sub> exposure. This  
 663 means that mass loss and exposure time are well correlated. Thus, % mass loss can be used to represent the extent  
 664 of aging.

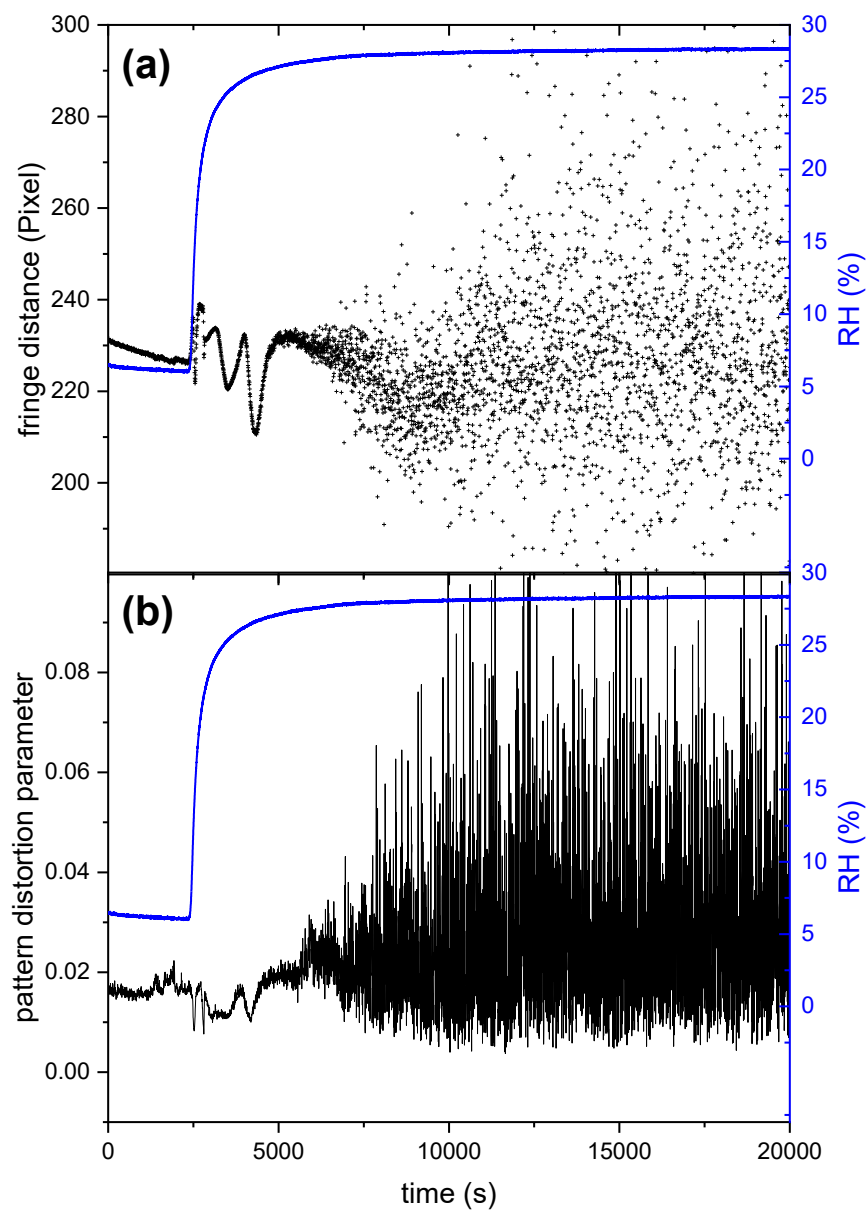




666 **Figure E-1: Viscosity of AA particles as a function of mass loss color-coded according to the exposure time (h) for (a)**  
667 **UV-exposure experiments and (b) UV+O<sub>3</sub>.**

668

669 **Appendix F. Mean fringe distance and pattern distortion parameter of AA particle exposed to UV and O<sub>3</sub> up to**  
670 **26% mass loss upon humidifying**





672 **Figure F-1: (a) Mean fringe distance and (b) pattern distortion parameter of AA particle exposed to UV and O<sub>3</sub> up to**  
 673 **26% mass loss upon increasing RH from 6.0% to 28.4%. Significant increase in fluctuations in fringe distance (a) and**  
 674 **pattern distortion parameter (b) are observed at 6,000 s, indicating the efflorescence of AA.**

675

676 **Data availability.** All data of the figures are available online at <https://doi.org/10.3929/ethz-c-000788184>  
 677 (Antossian et al., 2025).

678

679 **Author contributions.** Funding was acquired by UKK. Experiments were conceptualized by UKK and CA and  
 680 carried out by CA. The data were analyzed by CA and UKK. The manuscript was written by CA and revised by  
 681 UKK and MM.

682

683 **Competing interests.** The authors declare that they have no conflict of interest.

684

685

686

687 **Acknowledgements.** The authors would like to thank Colette Heald for providing helpful feedback on the  
 688 manuscript. The authors would like to acknowledge Kristopher McNeill and Oleksandr Yushchenko for their  
 689 assistance in the absorbance measurements.

690

691 **Financial support.** This research has been supported by the Eidgenössische Technische Hochschule Zürich (grant  
 692 no. 23-1 ETH-020)

693

694

695

## 696 References

- 697 Antossian, C., Müller, M., and Krieger, U. K.: Photochemical and ozone-induced aging  
 698 significantly alter the viscosity of aqueous trans-aconitic acid aerosol particles (Data collection),  
 699 ETH Research Collection [dataset], doi: 10.3929/ethz-c-000788184, 2025.
- 700 Athanasiadis, A., Fitzgerald, C., Davidson, N. M., Giorio, C., Botchway, S. W., Ward, A. D.,  
 701 Kalberer, M., Pope, F. D., and Kuimova, M. K.: Dynamic viscosity mapping of the oxidation of  
 702 squalene aerosol particles, *Phys. Chem. Chem. Phys.*, 18, 30385-30393,  
 703 doi:10.1039/c6cp05674a, 2016.
- 704 Baboosian, V. J., Crescenzo, G., Huang, Y. Z., Mahrt, F., Shiraiwa, M., Bertram, A. K., and  
 705 Nizkorodov, S. A.: Sunlight can convert atmospheric aerosols into a glassy solid state and modify  
 706 their environmental impacts, *Proc. Natl. Acad. Sci. U. S. A.*, 119, 10, doi:  
 707 10.1073/pnas.2208121119, 2022.
- 708 Bastelberger, S., Krieger, U. K., Luo, B. P., and Peter, T.: Diffusivity measurements of volatile  
 709 organics in levitated viscous aerosol particles, *Atmos. Chem. Phys.*, 17, 8453-8471,  
 710 doi:10.5194/acp-17-8453-2017, 2017.
- 711 Bones, D. L., Reid, J. P., Lienhard, D. M., and Krieger, U. K.: Comparing the mechanism of water  
 712 condensation and evaporation in glassy aerosol, *Proc. Natl. Acad. Sci. U. S. A.*, 109, 11613-  
 713 11618, doi:10.1073/pnas.1200691109, 2012.



- 714 Braun, C. and Krieger, U. K.: Two dimensional angular light scattering in aqueous NaCl single  
715 aerosol particles during deliquescence and efflorescence, *Opt. Express*, 8, 314-321,  
716 doi:10.1364/oe.8.000314, 2001.
- 717 Bruni, G. O. and Klasson, K. T.: Aconitic Acid Recovery from Renewable Feedstock and Review of  
718 Chemical and Biological Applications, *Foods*, 11, 18, doi:10.3390/foods11040573, 2022.
- 719 Chan, L. P. and Chan, C. K.: Roles of the Phase State and Water Content in Ozonolysis of Internal  
720 Mixtures of Maleic Acid and Ammonium Sulfate Particles, *Aerosol Sci. Technol.*, 46, 781-793,  
721 doi:10.1080/02786826.2012.665514, 2012.
- 722 Chan, M. N., Kreidenweis, S. M., and Chan, C. K.: Measurements of the hygroscopic and  
723 deliquescence properties of organic compounds of different solubilities in water and their  
724 relationship with cloud condensation nuclei activities, *Environ. Sci. Technol.*, 42, 3602-3608,  
725 doi:10.1021/es7023252, 2008.
- 726 Davies, J. F.: Mass, charge, and radius of droplets in a linear quadrupole electrodynamic  
727 balance, *Aerosol Sci. Technol.*, 53, 309-320, doi:10.1080/02786826.2018.1559921, 2019.
- 728 Davis, E. J. and Periasamy, R.: LIGHT-SCATTERING AND AERODYNAMIC SIZE MEASUREMENTS  
729 FOR HOMOGENEOUS AND INHOMOGENEOUS MICROSPHERES, *Langmuir*, 1, 373-379,  
730 doi:10.1021/la00063a020, 1985.
- 731 Debenedetti, P. G. and Stillinger, F. H.: Supercooled liquids and the glass transition, *Nature*, 410,  
732 259-267, doi:10.1038/35065704, 2001.
- 733 Dockery, D. W. and Pope, C. A.: ACUTE RESPIRATORY EFFECTS OF PARTICULATE AIR-  
734 POLLUTION, *Annu. Rev. Public Health*, 15, 107-132, doi:10.1146/annurev.pu.15.050194.000543,  
735 1994.
- 736 Dou, J., Alpert, P. A., Arroyo, P. C., Luo, B. P., Schneider, F., Xto, J., Huthwelker, T., Borca, C. N.,  
737 Henzler, K. D., Raabe, J., Watts, B., Herrmann, H., Peter, T., Ammann, M., and Krieger, U. K.:  
738 Photochemical degradation of iron(III) citrate/citric acid aerosol quantified with the combination  
739 of three complementary experimental techniques and a kinetic process model, *Atmos. Chem.*  
740 *Phys.*, 21, 315-338, doi:10.5194/acp-21-315-2021, 2021.
- 741 Duplissy, J., DeCarlo, P. F., Dommen, J., Alfarra, M. R., Metzger, A., Barmapadimos, I., Prevot, A. S.  
742 H., Weingartner, E., Tritscher, T., Gysel, M., Aiken, A. C., Jimenez, J. L., Canagaratna, M. R.,  
743 Worsnop, D. R., Collins, D. R., Tomlinson, J., and Baltensperger, U.: Relating hygroscopicity and  
744 composition of organic aerosol particulate matter, *Atmos. Chem. Phys.*, 11, 1155-1165,  
745 doi:10.5194/acp-11-1155-2011, 2011.
- 746 Einstein, A.: Über die von der molekularkinetischen Theorie der Wärme geforderte Bewegung  
747 von in ruhenden Flüssigkeiten suspendierten Teilchen, *Ann. Phys.*, 17, 549-560, 1905.
- 748 Evoy, E., Kamal, S., Patey, G. N., Martin, S. T., and Bertram, A. K.: Unified Description of Diffusion  
749 Coefficients from Small to Large Molecules in Organic-Water Mixtures, *J. Phys. Chem. A*, 124,  
750 2301-2308, doi:10.1021/acs.jpca.9b11271, 2020.
- 751 Gou, Y. F., Xie, M. J., and Chen, J.: The phase state and viscosity of organic aerosol and related  
752 impacts on atmospheric physicochemical processes: A review, *Atmos. Environ.*, 343, 17,  
753 doi:10.1016/j.atmosenv.2024.120985, 2025.
- 754 Han, S., Hong, J., Luo, Q. W., Xu, H. B., Tan, H. B., Wang, Q. Q., Tao, J. C., Zhou, Y. Q., Peng, L., He,  
755 Y., Shi, J. N., Ma, N., Cheng, Y. F., and Su, H.: Hygroscopicity of organic compounds as a function  
756 of organic functionality, water solubility, molecular weight, and oxidation level, *Atmos. Chem.*  
757 *Phys.*, 22, 3985-4004, doi:10.5194/acp-22-3985-2022, 2022.
- 758 Hildebrandt Ruiz, L., Paciga, A. L., Cerully, K. M., Nenes, A., Donahue, N. M., and Pandis, S. N.:  
759 Formation and aging of secondary organic aerosol from toluene: changes in chemical  
760 composition, volatility, and hygroscopicity, *Atmos. Chem. Phys.*, 15, 8301-8313,  
761 doi:10.5194/acp-15-8301-2015, 2015.
- 762 Hosny, N. A., Fitzgerald, C., Vynniauskas, A., Athanasiadis, A., Berkemeier, T., Uygur, N., Pöschl,  
763 U., Shiraiwa, M., Kalberer, M., Pope, F. D., and Kuimova, M. K.: Direct imaging of changes in  
764 aerosol particle viscosity upon hydration and chemical aging, *Chem. Sci.*, 7, 1357-1367,  
765 doi:10.1039/c5sc02959g, 2016.



766 Jakubczyk, D., Derkachov, G., Kolwas, M., and Kolwas, K.: Combining weighting and  
767 scatterometry: Application to a levitated droplet of suspension, *J. Quant. Spectrosc. Radiat.*  
768 *Transf.*, 126, 99-104, doi:10.1016/j.jqsrt.2012.11.010, 2013.

769 Jimenez, J. L., Canagaratna, M. R., Donahue, N. M., Prevot, A. S. H., Zhang, Q., Kroll, J. H.,  
770 DeCarlo, P. F., Allan, J. D., Coe, H., Ng, N. L., Aiken, A. C., Docherty, K. S., Ulbrich, I. M., Grieshop,  
771 A. P., Robinson, A. L., Duplissy, J., Smith, J. D., Wilson, K. R., Lanz, V. A., Hueglin, C., Sun, Y. L.,  
772 Tian, J., Laaksonen, A., Raatikainen, T., Rautiainen, J., Vaattovaara, P., Ehn, M., Kulmala, M.,  
773 Tomlinson, J. M., Collins, D. R., Cubison, M. J., Dunlea, E. J., Huffman, J. A., Onasch, T. B., Alfarra,  
774 M. R., Williams, P. I., Bower, K., Kondo, Y., Schneider, J., Drewnick, F., Borrmann, S., Weimer, S.,  
775 Demerjian, K., Salcedo, D., Cottrell, L., Griffin, R., Takami, A., Miyoshi, T., Hatakeyama, S.,  
776 Shimono, A., Sun, J. Y., Zhang, Y. M., Dzepina, K., Kimmel, J. R., Sueper, D., Jayne, J. T., Herndon,  
777 S. C., Trimborn, A. M., Williams, L. R., Wood, E. C., Middlebrook, A. M., Kolb, C. E., Baltensperger,  
778 U., and Worsnop, D. R.: Evolution of Organic Aerosols in the Atmosphere, *Science*, 326, 1525-  
779 1529, doi:10.1126/science.1180353, 2009.

780 Kalberer, M., Paulsen, D., Sax, M., Steinbacher, M., Dommen, J., Prevot, A. S. H., Fisseha, R.,  
781 Weingartner, E., Frankevich, V., Zenobi, R., and Baltensperger, U.: Identification of polymers as  
782 major components of atmospheric organic aerosols, *Science*, 303, 1659-1662,  
783 doi:10.1126/science.1092185, 2004.

784 Kanakidou, M., Seinfeld, J. H., Pandis, S. N., Barnes, I., Dentener, F. J., Facchini, M. C., Van  
785 Dingenen, R., Ervens, B., Nenes, A., Nielsen, C. J., Swietlicki, E., Putaud, J. P., Balkanski, Y., Fuzzi,  
786 S., Horth, J., Moortgat, G. K., Winterhalter, R., Myhre, C. E. L., Tsigaridis, K., Vignati, E.,  
787 Stephanou, E. G., and Wilson, J.: Organic aerosol and global climate modelling: a review, *Atmos.*  
788 *Chem. Phys.*, 5, 1053-1123, doi:10.5194/acp-5-1053-2005, 2005.

789 Koop, T., Bookhold, J., Shiraiwa, M., and Pöschl, U.: Glass transition and phase state of organic  
790 compounds: dependency on molecular properties and implications for secondary organic  
791 aerosols in the atmosphere, *Phys. Chem. Chem. Phys.*, 13, 19238-19255,  
792 doi:10.1039/c1cp22617g, 2011.

793 Krieger, U. K., Siegrist, F., Marcolli, C., Emanuelsson, E. U., Gobel, F. M., Bilde, M., Marsh, A.,  
794 Reid, J. P., Huisman, A. J., Riipinen, I., Hyttinen, N., Myllys, N., Kurtén, T., Bannan, T., Percival, C.  
795 J., and Topping, D.: A reference data set for validating vapor pressure measurement techniques:  
796 homologous series of polyethylene glycols, *Atmos. Meas. Tech.*, 11, 49-63, doi:10.5194/amt-11-  
797 49-2018, 2018.

798 Kroll, J. H. and Seinfeld, J. H.: Chemistry of secondary organic aerosol: Formation and evolution  
799 of low-volatility organics in the atmosphere, *Atmos. Environ.*, 42, 3593-3624,  
800 doi:10.1016/j.atmosenv.2008.01.003, 2008.

801 Kroll, J. H., Lim, C. Y., Kessler, S. H., and Wilson, K. R.: Heterogeneous Oxidation of Atmospheric  
802 Organic Aerosol: Kinetics of Changes to the Amount and Oxidation State of Particle-Phase  
803 Organic Carbon, *J. Phys. Chem. A*, 119, 10767-10783, doi:10.1021/acs.jpca.5b06946, 2015.

804 Kroll, J. H., Donahue, N. M., Jimenez, J. L., Kessler, S. H., Canagaratna, M. R., Wilson, K. R.,  
805 Altieri, K. E., Mazzoleni, L. R., Wozniak, A. S., Bluhm, H., Mysak, E. R., Smith, J. D., Kolb, C. E.,  
806 and Worsnop, D. R.: Carbon oxidation state as a metric for describing the chemistry of  
807 atmospheric organic aerosol, *Nat. Chem.*, 3, 133-139, doi:10.1038/nchem.948, 2011.

808 Lambe, A. T., Onasch, T. B., Massoli, P., Croasdale, D. R., Wright, J. P., Ahern, A. T., Williams, L.  
809 R., Worsnop, D. R., Brune, W. H., and Davidovits, P.: Laboratory studies of the chemical  
810 composition and cloud condensation nuclei (CCN) activity of secondary organic aerosol (SOA)  
811 and oxidized primary organic aerosol (OPOA), *Atmos. Chem. Phys.*, 11, 8913-8928,  
812 doi:10.5194/acp-11-8913-2011, 2011.

813 Lienhard, D. M., Bones, D. L., Zuend, A., Krieger, U. K., Reid, J. P., and Peter, T.: Measurements of  
814 Thermodynamic and Optical Properties of Selected Aqueous Organic and Organic-Inorganic  
815 Mixtures of Atmospheric Relevance, *J. Phys. Chem. A*, 116, 9954-9968, doi:10.1021/jp3055872,  
816 2012.



- 817 Marcolli, C. and Krieger, U. K.: Relevance of Particle Morphology for Atmospheric Aerosol  
818 Processing, *Trends Chem.*, 2, 1-3, doi:10.1016/j.trechm.2019.11.008, 2020.
- 819 Marcolli, C., Luo, B. P., Peter, T., and Wienhold, F. G.: Internal mixing of the organic aerosol by gas  
820 phase diffusion of semivolatile organic compounds, *Atmos. Chem. Phys.*, 4, 2593-2599,  
821 doi:10.5194/acp-4-2593-2004, 2004.
- 822 Mu, Q., Shiraiwa, M., Octaviani, M., Ma, N., Ding, A. J., Su, H., Lammel, G., Pöschl, U., and  
823 Cheng, Y. F.: Temperature effect on phase state and reactivity controls atmospheric multiphase  
824 chemistry and transport of PAHs, *Sci. Adv.*, 4, 8, doi:10.1126/sciadv.aap7314, 2018.
- 825 Muller, G. T. A. and Stokes, R. H.: THE MOBILITY OF THE UNDISSOCIATED CITRIC ACID  
826 MOLECULE IN AQUEOUS SOLUTION, *Transactions of the Faraday Society*, 53, 642-645,  
827 doi:10.1039/tf9575300642, 1957.
- 828 Müller, M., Mishra, A., Berkemeier, T., Hausammann, E., Peter, T., and Krieger, U. K.:  
829 Electrodynamical balance-mass spectrometry reveals impact of oxidant concentration on  
830 product composition in the ozonolysis of oleic acid, *Phys. Chem. Chem. Phys.*, 24, 27086-  
831 27104, doi:10.1039/d2cp03289a, 2022.
- 832 Murray, B. J., Wilson, T. W., Dobbie, S., Cui, Z. Q., Al-Jumur, S., Möhler, O., Schnaiter, M., Wagner,  
833 R., Benz, S., Niemand, M., Saathoff, H., Ebert, V., Wagner, S., and Kärcher, B.: Heterogeneous  
834 nucleation of ice particles on glassy aerosols under cirrus conditions, *Nat. Geosci.*, 3, 233-237,  
835 doi:10.1038/ngeo817, 2010.
- 836 Nel, A.: Air pollution-related illness: Effects of particles, *Science*, 308, 804-806,  
837 doi:10.1126/science.1108752, 2005.
- 838 O'Brien, R. E. and Kroll, J. H.: Photolytic Aging of Secondary Organic Aerosol: Evidence for a  
839 Substantial Photo-Recalcitrant Fraction, *J. Phys. Chem. Lett.*, 10, 4003-4009,  
840 doi:10.1021/acs.jpclett.9b01417, 2019.
- 841 O'Meara, S., Topping, D. O., and McFiggans, G.: The rate of equilibration of viscous aerosol  
842 particles, *Atmos. Chem. Phys.*, 16, 5299-5313, doi:10.5194/acp-16-5299-2016, 2016.
- 843 Pang, X. F.: *Water: Molecular Structure and Properties*, World Scientific Publishing Co. Pte. Ltd.,  
844 doi:10.1142/8669, 2014.
- 845 Pankow, J. F.: AN ABSORPTION-MODEL OF THE GAS AEROSOL PARTITIONING INVOLVED IN THE  
846 FORMATION OF SECONDARY ORGANIC AEROSOL, *Atmos. Environ.*, 28, 189-193,  
847 doi:10.1016/1352-2310(94)90094-9, 1994.
- 848 Petters, M. D. and Kreidenweis, S. M.: A single parameter representation of hygroscopic growth  
849 and cloud condensation nucleus activity, *Atmos. Chem. Phys.*, 7, 1961-1971, doi:10.5194/acp-7-  
850 1961-2007, 2007.
- 851 Pope, F. D., Gallimore, P. J., Fuller, S. J., Cox, R. A., and Kalberer, M.: Ozonolysis of Maleic Acid  
852 Aerosols: Effect upon Aerosol Hygroscopicity, Phase and Mass, *Environ. Sci. Technol.*, 44, 6656-  
853 6660, doi:10.1021/es1008278, 2010.
- 854 Pöschl, U. and Shiraiwa, M.: Multiphase Chemistry at the Atmosphere-Biosphere Interface  
855 Influencing Climate and Public Health in the Anthropocene, *Chem. Rev.*, 115, 4440-4475,  
856 doi:10.1021/cr500487s, 2015.
- 857 Price, H. C., Mattsson, J., Zhang, Y., Bertram, A. K., Davies, J. F., Grayson, J. W., Martin, S. T.,  
858 O'Sullivan, D., Reid, J. P., Rickards, A. M. J., and Murray, B. J.: Water diffusion in atmospherically  
859 relevant  $\alpha$ -pinene secondary organic material, *Chem. Sci.*, 6, 4876-4883,  
860 doi:10.1039/c5sc00685f, 2015.
- 861 Rickards, A. M. J., Miles, R. E. H., Davies, J. F., Marshall, F. H., and Reid, J. P.: Measurements of  
862 the Sensitivity of Aerosol Hygroscopicity and the  $\kappa$  Parameter to the O/C Ratio, *J. Phys. Chem. A*,  
863 117, 14120-14131, doi:10.1021/jp407991n, 2013.
- 864 Rickards, A. M. J., Song, Y. C., Miles, R. E. H., Preston, T. C., and Reid, J. P.: Variabilities and  
865 uncertainties in characterising water transport kinetics in glassy and ultraviscous aerosol, *Phys.*  
866 *Chem. Chem. Phys.*, 17, 10059-10073, doi:10.1039/c4cp05383d, 2015.
- 867 Romonosky, D. E., Laskin, A., Laskin, J., and Nizkorodov, S. A.: High-Resolution Mass  
868 Spectrometry and Molecular Characterization of Aqueous Photochemistry Products of Common





- 869 Types of Secondary Organic Aerosols, *J. Phys. Chem. A*, 119, 2594-2606, doi:10.1021/jp509476r,  
870 2015.
- 871 Rothfuss, N. E. and Petters, M. D.: Influence of Functional Groups on the Viscosity of Organic  
872 Aerosol, *Environ. Sci. Technol.*, 51, 271-279, doi:10.1021/acs.est.6b04478, 2017.
- 873 Seinfeld, J. H. and Pandis, S. N.: Atmospheric chemistry and physics: from air pollution to  
874 climate change, Third Edition, John Wiley & Sons, Inc., ISBN: 9781119221166, 2016.
- 875 Shiraiwa, M., Ammann, M., Koop, T., and Pöschl, U.: Gas uptake and chemical aging of semisolid  
876 organic aerosol particles, *Proc. Natl. Acad. Sci. U. S. A.*, 108, 11003-11008,  
877 doi:10.1073/pnas.1103045108, 2011.
- 878 Shrivastava, M., Lou, S., Zelenyuk, A., Easter, R. C., Corley, R. A., Thrall, B. D., Rasch, P. J., Fast, J.  
879 D., Simonich, S. L. M., Shen, H. Z., and Tao, S.: Global long-range transport and lung cancer risk  
880 from polycyclic aromatic hydrocarbons shielded by coatings of organic aerosol, *Proc. Natl.*  
881 *Acad. Sci. U. S. A.*, 114, 1246-1251, doi:10.1073/pnas.1618475114, 2017.
- 882 Song, Y. C., Haddrell, A. E., Bzdek, B. R., Reid, J. P., Barman, T., Topping, D. O., Percival, C., and  
883 Cai, C.: Measurements and Predictions of Binary Component Aerosol Particle Viscosity, *J. Phys.*  
884 *Chem. A*, 120, 8123-8137, doi:10.1021/acs.jpca.6b07835, 2016.
- 885 Steimer, S. S., Krieger, U. K., Te, Y. F., Lienhard, D. M., Huisman, A. J., Luo, B. P., Ammann, M., and  
886 Peter, T.: Electrodynamic balance measurements of thermodynamic, kinetic, and optical aerosol  
887 properties inaccessible to bulk methods, *Atmos. Meas. Tech.*, 8, 2397-2408, doi:10.5194/amt-8-  
888 2397-2015, 2015.
- 889 Steiner, B., Berge, B., Gausmann, R., Rohmann, J., and Rühl, E.: Fast in situ sizing technique for  
890 single levitated liquid aerosols, *Appl. Optics*, 38, 1523-1529, doi:10.1364/ao.38.001523, 1999.
- 891 Sun, M. R. and Smith, G. D.: Photolytic Mass Loss of Humic Substances Measured with a Quartz  
892 Crystal Microbalance, *ACS Earth Space Chem.*, 8, 1623-1633,  
893 doi:10.1021/acsearthspacechem.4c00134, 2024.
- 894 Willis, M. D. and Wilson, K. R.: Coupled Interfacial and Bulk Kinetics Govern the Timescales of  
895 Multiphase Ozonolysis Reactions, *J. Phys. Chem. A*, 126, 4991-5010,  
896 doi:10.1021/acs.jpca.2c03059, 2022.
- 897 Wolf, M. J., Zhang, Y., Zawadowicz, M. A., Goodell, M., Froyd, K., Freney, E., Sellegri, K., Rösch,  
898 M., Cui, T. Q., Winter, M., Lacher, L., Axisa, D., DeMott, P. J., Levin, E. J. T., Gute, E., Abbatt, J.,  
899 Koss, A., Kroll, J. H., Surratt, J. D., and Cziczo, D. J.: A biogenic secondary organic aerosol source  
900 of cirrus ice nucleating particles, *Nat. Commun.*, 11, 9, doi:10.1038/s41467-020-18424-6, 2020.
- 901 Zardini, A. A., Krieger, U. K., and Marcolli, C.: White light Mie resonance spectroscopy used to  
902 measure very low vapor pressures of substances in aqueous solution aerosol particles, *Opt.*  
903 *Express*, 14, 6951-6962, doi:10.1364/oe.14.006951, 2006.
- 904 Zardini, A. A., Sjogren, S., Marcolli, C., Krieger, U. K., Gysel, M., Weingartner, E., Baltensperger,  
905 U., and Peter, T.: A combined particle trap/HTDMA hygroscopicity study of mixed  
906 inorganic/organic aerosol particles, *Atmos. Chem. Phys.*, 8, 5589-5601, doi:10.5194/acp-8-  
907 5589-2008, 2008.
- 908 Zhang, Q., Jimenez, J. L., Canagaratna, M. R., Allan, J. D., Coe, H., Ulbrich, I., Alfarra, M. R.,  
909 Takami, A., Middlebrook, A. M., Sun, Y. L., Dzepina, K., Dunlea, E., Docherty, K., DeCarlo, P. F.,  
910 Salcedo, D., Onasch, T., Jayne, J. T., Miyoshi, T., Shimono, A., Hatakeyama, S., Takegawa, N.,  
911 Kondo, Y., Schneider, J., Drewnick, F., Borrmann, S., Weimer, S., Demerjian, K., Williams, P.,  
912 Bower, K., Bahreini, R., Cottrell, L., Griffin, R. J., Rautiainen, J., Sun, J. Y., Zhang, Y. M., and  
913 Worsnop, D. R.: Ubiquity and dominance of oxygenated species in organic aerosols in  
914 anthropogenically-influenced Northern Hemisphere midlatitudes, *Geophys. Res. Lett.*, 34, 6,  
915 doi:10.1029/2007gl029979, 2007.
- 916 Zobrist, B., Soonsin, V., Luo, B. P., Krieger, U. K., Marcolli, C., Peter, T., and Koop, T.: Ultra-slow  
917 water diffusion in aqueous sucrose glasses, *Phys. Chem. Chem. Phys.*, 13, 3514-3526,  
918 doi:10.1039/c0cp01273d, 2011.



919 Zuend, A., Marcolli, C., Luo, B. P., and Peter, T.: A thermodynamic model of mixed organic-  
920 inorganic aerosols to predict activity coefficients, *Atmos. Chem. Phys.*, 8, 4559-4593,  
921 doi:10.5194/acp-8-4559-2008, 2008.  
922 Zuend, A., Marcolli, C., Booth, A. M., Lienhard, D. M., Soonsin, V., Krieger, U. K., Topping, D. O.,  
923 McFiggans, G., Peter, T., and Seinfeld, J. H.: New and extended parameterization of the  
924 thermodynamic model AIOMFAC: calculation of activity coefficients for organic-inorganic  
925 mixtures containing carboxyl, hydroxyl, carbonyl, ether, ester, alkenyl, alkyl, and aromatic  
926 functional groups, *Atmos. Chem. Phys.*, 11, 9155-9206, doi:10.5194/acp-11-9155-2011, 2011.  
927